

AD-A250 814



WL-TR-91-3089



An Examination of Several High Resolution Schemes Applied to Complex Problems in High Speed Flows

Norbert Kroll *Dozent für Aerodynamik und Flugmechanik*
DLR, Institute for Design Aerodynamics
Flughafen, D-3300 Braunschweig, West Germany

Michael Aftosmis and Datta Gaitonde
U.S. Air Force Wright Research and Development Center
Wright-Patterson Air Force Base, OH 45433

February 1992

2
DTIC
ELECTED
MAY 19 1992
S, D

Final Report for Period June 1991 - December 1991

Approved for public release; distribution unlimited.

FLIGHT DYNAMICS DIRECTORATE
WRIGHT LABORATORY
AIR FORCE SYSTEMS COMMAND
WRIGHT-PATTERSON AIR FORCE BASE, OHIO 45433-6553

92-13258



42 10 386

NOTICE

When Government drawings, specifications, or other data are used for any purpose other than in connection with a definitely Government-related procurement, the United States Government incurs no responsibility or any obligation whatsoever. The fact that the government may have formulated or in any way supplied the said drawings, specifications, or other data, is not to be regarded by implication, or otherwise in any manner construed, as licensing the holder, or any other person or corporation; or as conveying any rights or permission to manufacture, use, or sell any patented invention that may in any way be related thereto.

This report is releasable to the National Technical Information Service (NTIS). At NTIS, it will be available to the general public, including foreign nations.

This technical report has been reviewed and is approved for publication.

102
MICHAEL J. AFTOSMIS, Capt USAF
Computational Gasdynamicist

Dennis Sedlock
DENNIS SEDLOCK, Chief
Aerodynamics & Airframe Branch

Robert L. Herklotz
ROBERT L. HERKLOTZ, Col, USAF
Chief
Aeromechanics Division

W. May Davis
JAMES J. OLSEN
Chief Scientist
Flight Dynamics

If your address has changed, if you wish to be removed from our mailing list, or if the addressee is no longer employed by your organization please notify WL/FIMM, WPAFB, OH 45433-6553 to help us maintain a current mailing list.

Copies of this report should not be returned unless return is required by security considerations, contractual obligations, or notice on a specific document.

REPORT DOCUMENTATION PAGE

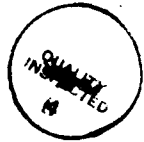
Form Approved
OMB No. 0704-0188

Public reporting burden for this collection of information is estimated to average 1 hour per response, including the time for reviewing instructions, searching existing data sources, gathering and maintaining the data needed, and completing and reviewing the collection of information. Send comments regarding this burden estimate or any other aspect of this collection of information, including suggestions for reducing this burden, to Washington Headquarters Services, Directorate for Information Operations and Reports, 1215 Jefferson Davis Highway, Suite 1204, Arlington, VA 22202-4302, and to the Office of Management and Budget, Paperwork Reduction Project (0704-0188), Washington, DC 20503.

1. AGENCY USE ONLY (Leave blank)	2. REPORT DATE	3. REPORT TYPE AND DATES COVERED	
	2 Feb 92	Final Report	Jun 91 - Dec 91
4. TITLE AND SUBTITLE		5. FUNDING NUMBERS	
An Examination of Several High Resolution Schemes Applied to Complex Problems in High Speed Flows		PE: 616100 P: 2307 T: N6 UN: 11	
6. AUTHOR(S)		8. PERFORMING ORGANIZATION REPORT NUMBER	
Norbert Kroll Michael Aftosmis Datta Gaitonde			
7. PERFORMING ORGANIZATION NAME(S) AND ADDRESS(ES)		9. SPONSORING/MONITORING AGENCY NAME(S) AND ADDRESS(ES)	
DLR, Institute for Design Aerodynamics Flughafen, D-3300 Braunschweig, Germany		Dr Joseph Shang, (513) 255-7127 Flight Dynamics Laboratory (WL/FIMM) Wright Laboratory Wright-Patterson AFB OH 45433-6553	
10. SPONSORING/MONITORING AGENCY REPORT NUMBER			
WL-TR-91-3089			
11. SUPPLEMENTARY NOTES			
12a. DISTRIBUTION/AVAILABILITY STATEMENT		12b. DISTRIBUTION CODE	
Approved for public release; distribution is unlimited.			
13. ABSTRACT (Maximum 200 words)			
A comparative study of five upwind schemes was performed to evaluate their ability to accurately model the convective fluxes of the Euler equations for problems containing complex shock structure. The schemes investigated used a variety of Riemann solvers and obtained higher order accuracy using either a MUSCL or non-MUSCL approach. The MUSCL-type schemes included the flux vector split formulations of Steiger-Warming and van Leer and the flux difference split approach of Roe. The Non-MUSCL schemes included the "Symmetric" and "Upwind" TVD methods of Yee, and Harten and Yee. Two central difference schemes provide a basis for the evaluation of these upwind methods. The comparison was performed using identical meshes and convergence criteria. In a supersonic blunt body flow, all the upwind schemes displayed comparably resolved bow shocks, independent of free stream Mach number. However, a complex type IV shock on cowl lip example pointed out significant difference in the accuracy and convergence behavior of the schemes. A comparison of the flow structure shown by the various algorithms on identical grids indicated that the discrete solutions obtained with Upwind-TVD and Roe flux difference splitting were the least diffusive of the upwind methods considered.			
14. SUBJECT TERMS		15. NUMBER OF PAGES	
Upwind Schemes, Euler Flows, Types IV Interactions Flux-Splitting, TVD		63	
16. PRICE CODE			
17. SECURITY CLASSIFICATION OF REPORT	18. SECURITY CLASSIFICATION OF THIS PAGE	19. SECURITY CLASSIFICATION OF ABSTRACT	20. LIMITATION OF ABSTRACT
Unclassified	Unclassified	Unclassified	UL

Contents

List of Figures	iv
List of Tables	vi
Acknowledgements	vii
1 Introduction	1
2 Brief Description of Schemes Investigated	4
3 Overview and Classification of Computations	9
3.1 Criteria for Comparison	11
4 Results	12
4.0.1 Case A - Blunt Body	12
4.0.2 Case B - Type IV Interference Flow	13
5 Conclusion	20
6 References	21
Nomenclature	26



Accession For	
NTIS GRA&I	<input checked="" type="checkbox"/>
DTIC TAB	<input type="checkbox"/>
Unannounced	<input type="checkbox"/>
Justification	
By _____	
Distribution/	
Availability Codes	
Dist	Avail and/or
	Special
A-1	

List of Figures

1	Schematic of Type IV shock-shock interaction of Edney [28] . Angles of shocks and shear layers calculated from oblique shock relations and hodograph methods of [44] .	28
2	Residual convergence behavior for a blunt body on a 40x40 grid at Mach 8.03.	29
3	RMS surface pressure behavior for a blunt body on a 40x40 grid at Mach 8.03.	30
4	Mach contours for blunt body on a 40 × 40 grid at Mach 8.03.	31
5	Mach number vs. grid point for a blunt body on a 40 × 40 grid at Mach 8.03 along the centerline.	32
6	Mach number vs. grid point for a blunt body on a 40 × 40 grid at Mach 8.03 along a ray inclined at 36° to the vertical.	33
7	Mach number vs. grid point for a blunt body on a 40 × 40 grid at Mach 16.33 along the centerline.	34
8	Mach Number vs. grid point for a blunt body on a 40 × 40 grid at Mach 16.33 along a ray inclined at 36° degrees to the vertical.	35
9	Stagnation enthalpy losses along the stagnation streamline on 20 × 20 and 40 × 40 grids for Mach 8.03.	36
10	Residual convergence behavior for Type IV interaction on coarse (60 × 40) grid.	37
11	RMS surface pressure convergence behavior for Type IV interaction on coarse (60 × 40) grid.	38
12	Mach contour plots for Type IV interaction on coarse (60 × 40) grid, $M_\infty = 8.03$	39
13	Mach contours at various extrema in convergence cycle for Lax-Wendroff scheme with dissipation reduced to blunt body levels and CFL number reduced by 10 (60×40 grid, $M_\infty = 8.03$).	41
14	Surface pressure comparison for Type IV interaction on coarse (60 × 40) grid $M_\infty = 8.03$	42
15	Residual convergence behavior for Type IV interaction on medium (120 × 80) grid, $M_\infty = 8.03$	43

16	RMS surface pressure convergence behavior for Type IV interaction on medium (120 \times 80) mesh, $M_{\infty} = 8.03$.	44
17	Convergence behavior of van Leer scheme with explicit and implicit time integration for Type IV interaction, $M_{\infty} = 8.03$.	45
18	Mach contour plots for Type IV interaction on medium (120 \times 80) grid, $M_{\infty} = 8.03$	46
19	Velocity vectors of typical solution of Type IV interaction on a medium (120 \times 80) grid (Upwind TVD), $M_{\infty} = 8.03$.	48
20	Representative "particle traces" from Upwind TVD scheme on medium (120 \times 80) grid, $M_{\infty} = 8.03$.	49
21	Surface pressure comparison for Type IV interaction on medium (120 \times 80) grid, $M_{\infty} = 8.03$.	50
22	Mach contours at various extrema in convergence cycle for Upwind TVD scheme on medium (120 \times 80) grid, $M_{\infty} = 8.03$.	51
23	Surface pressure at various extrema in convergence cycle for Upwind TVD scheme on medium (120 \times 80) grid, $M_{\infty} = 8.03$.	52
24	Convergence behavior for Type IV interaction on fine (240 \times 160) grid, $M_{\infty} = 8.03$. Upper: Residual, Lower: RMS surface pressure.	53
25	Mach contour plots for Type IV interaction on fine (240 \times 160) grid for van Leer splitting and Symmetric TVD at 50 T_c , $M_{\infty} = 8.03$.	54
26	Schematic of solutions showing reflected oblique shock pattern in the supersonic layer over the body	55

List of Tables

1.1	Brief description of schemes and their nomenclature	3
3.1	Classification of computations for flow past a 2-D cylinder	10

Acknowledgements

Computations were performed on computers at WPAFB and the NAS program. The support and assistance of the staff at both locations are gratefully acknowledged.

1. Introduction

Recent interest in high Mach number flow has pointed out deficiencies of classical central difference schemes near strong discontinuities. While these schemes perform admirably in sub-, trans- and even low supersonic flows [1, 2, 3, 4, 5], problems arise due to oscillations which may grow unbounded in the vicinity of strong shocks. Inaccuracies due to the excess artificial dissipation required to suppress this behavior led to the development of a variety of upwind-biased schemes. These schemes rely on local wave propagation theory in differencing the convective terms of the governing equations throughout the domain.

The focus of the current effort is to investigate the characteristics of several upwind schemes for problems of realistic complexity in high speed flows against the backdrop of classical central difference techniques. Upwind schemes for the Euler and Navier-Stokes equations may be distinguished by the approximate Riemann solver used to evaluate the fluxes at the cell faces and the mechanism through which they obtain higher order spatial accuracy [6, 7, 8].

The approximate Riemann schemes of Roe [9], Osher [10], van Leer [11] and Steger-Warming [12] currently enjoy wide use within the research community. These solvers are extended to higher than first order through either a MUSCL [13] or non-MUSCL approach [8, 14]. For a non-linear scalar equation or a linear system of equations, schemes developed with either approach may also be TVD through the incorporation of an appropriately constructed flux limiter.

The concurrent development of many of these algorithms has led to several comparisons of similar schemes [13, 15, 16] or comparisons of a variety of schemes for simple problems [17, 18, 19, 20, 21, 22]. However, little effort has been made to study a wide class of schemes in a controlled setting on rigorous problems.

This led to the current work which examines several MUSCL and non-MUSCL schemes with a variety of Riemann solvers (Table 1.1) for a realistically complex configuration. These schemes are compared with central schemes using second and fourth order artificial damping. The shock on cowl lip problem, which was investigated experimentally by Holden *et al.* [23], has received much attention in recent literature [24, 25, 26, 27] and provides a rigorous test case of practical

importance. Edney [28] classified shock interference patterns into six types. The actual pattern established in any particular case depends primarily upon the strength and location of the impinging shock, the characteristics of the incoming flow and the cowl shape. Edney predicted the highest mechanical and thermal loading in the Type IV interaction which establishes itself when the impinging shock intersects the subsonic portion of the cowl bow shock. Figure 1 contains a schematic of the Type IV interaction that was investigated experimentally by Wieting and Holden [29]. A supersonic viscous shear layer emanates from the point of impingement. This layer forms a "jet" which strikes the body after passing through a terminating bow shock. Since inviscid features dominate this flow, the investigation is free to focus on the discretization of the inviscid terms only. This problem includes strong shocks and shear layers interacting in the presence of a body. These phenomena create many length scales in the flow and the shocks and shear layers are not necessarily aligned with the grid [23]. Furthermore, under certain circumstances, a weak instability arises in the interaction which may or may not be damped out by the truncation error of a given numerical method [25, 30].

The present work compares all schemes on identical grid systems at three levels of refinement. Particular emphasis is placed on convergence and accuracy of the algorithms under consideration.

Scheme No.	Spatial Discretization
1	Central differencing (5-point operator) + 2nd and 4th order dissipation
2	Central differencing (9-point operator) + 2nd and 4th order dissipation
3	Steger-Warming flux vector splitting + MUSCL
4	van Leer flux vector splitting + MUSCL
5	Roe flux difference splitting +MUSCL
6	“Symmetric” TVD of Yee (non-MUSCL)
7	“Upwind” TVD based on Harten and Yee (non-MUSCL)

Scheme	Limiter	Time Integration Scheme	Reference
1	—	Explicit Runge-Kutta scheme	[31]
2	—	Explicit Lax Wendroff	[32]
3	Minmod limiter	Gauss-Seidel line relaxation	[12, 33]
4	Minmod limiter	Gauss-Seidel line relaxation	[11, 33]
5	van Albada limiter	Explicit Runge-Kutta scheme	[9, 8]
6	Limiter (Ref. [8],Eqn. 3.51h)	Explicit Runge-Kutta scheme	[34, 35]
7	Limiter (Ref. [8],Eqn. 3.51f)	Explicit Runge-Kutta scheme	[36, 35]

Table 1.1: Brief description of schemes and their nomenclature

2. Brief Description of Schemes Investigated

In discretizing the Navier-Stokes equations, virtually all schemes rely on a centered approximation of the viscous terms. In an effort to focus solely on the convective flux approximation of these upwind schemes, this investigation considers the Euler equations. Additionally, excluding the viscous terms removes the diffusive loss mechanism from the governing equations and provides a homenthalpic reference state which may be used to assess the accuracy of the various methods. Writing the Euler equations in conservation form:

$$\frac{\partial \vec{U}}{\partial t} + \frac{\partial \vec{F}}{\partial x} + \frac{\partial \vec{G}}{\partial y} = 0 \quad (2.1)$$

\vec{U} is the solution vector of conserved variables and \vec{F} and \vec{G} are the flux vectors. The gas is assumed to be calorically perfect governed by the equation of state $p = \rho RT$ where p is the pressure, ρ the density, R the gas constant and T the static temperature.

This study focuses on the performance of MUSCL and non-MUSCL higher order upwind schemes. Suppressing the vector notation, denoting U^L and U^R as the left and right states, a brief description of each algorithm follows with reference to the evaluation of the inviscid flux at the cell surface $i + \frac{1}{2}$.

MUSCL Type Upwind Schemes

The MUSCL type schemes considered include Steger-Warming and van Leer flux vector splitting and Roe flux difference splitting.

• Steger-Warming flux vector splitting [12]:

The Steger-Warming flux vector splitting scheme may be written as:

$$F_{i+\frac{1}{2}} = F^+(U_{i+\frac{1}{2}}^L) + F^-(U_{i+\frac{1}{2}}^R) \quad (2.2)$$

With $A = \partial F / \partial U$,

$$A = R^{-1} \Lambda R = R^{-1} (\Lambda^+ + \Lambda^-) R = A^+ + A^- \quad (2.3)$$

$$F^+(U) = A^+U, \quad F^-(U) = A^-U \quad (2.4)$$

Here Λ is a diagonal matrix consisting of the eigenvalues of A , Λ^+ and Λ^- denote the splitting of the eigenvalues into positive and negative components and R is the similarity transformation diagonalizing A . The MUSCL approach [13] brings U^L and U^R to second order accuracy:

$$U_{i+\frac{1}{2}}^R = U_{i+1} - \frac{1}{2} \tilde{\Delta}_{i+\frac{1}{2}} \quad (2.5)$$

$$U_{i+\frac{1}{2}}^L = U_i + \frac{1}{2} \tilde{\Delta}_{i+\frac{1}{2}} \quad (2.6)$$

where:

$$\tilde{\Delta}_{i+\frac{1}{2}} = \text{minmod}(\Delta_{i+\frac{1}{2}}, \Delta_{i-\frac{1}{2}}) \quad (2.7)$$

and $\Delta_{i+\frac{1}{2}} = U^R - U^L$. With the addition of the minmod limiter, the algorithm reverts to first order accuracy at shocks in order to preserve monotonicity within of the solution.

• van Leer flux vector splitting [11]:

The functional form of the van Leer scheme is identical to the Steger-Warming algorithm (Eqn. 2.2) and, in fact, for supersonic flow the evaluation remains unchanged. For subsonic flow, F^\pm were revised by van Leer to avoid the discontinuity exhibited across sonic lines by the Steger-Warming algorithm. Denoting the Mach number normal to the interface as M_x , for subsonic flow ($|M_x| < 1$),

$$F^\pm = \left\{ \begin{array}{l} \pm \rho a \left\{ \frac{1}{2} (M_x \pm 1) \right\}^2 = f_1^\pm \\ f_1^\pm \frac{(\gamma-1)u \pm 2a}{\gamma} \\ f_1^\pm v \\ f_1^\pm \left[\frac{((\gamma-1)u \pm 2a)^2}{2(\gamma^2-1)} + \frac{v^2}{2} \right] \end{array} \right\} \quad (2.8)$$

This scheme also obtains second order accuracy with the MUSCL approach (Eqns. 2.5 through 2.7). Both Steger-Warming and van Leer methods utilize the cell-centered finite volume approach in transformed space [37].

- Roe's flux difference splitting [9]:

The Roe flux difference splitting reads as follows:

$$F_{i+\frac{1}{2}} = \frac{1}{2} \left[F \left(U_{i+\frac{1}{2}}^L \right) + F \left(U_{i+\frac{1}{2}}^R \right) \right] - \frac{1}{2} \hat{R}_{i+\frac{1}{2}} |\hat{\Lambda}_{i+\frac{1}{2}}| \hat{R}_{i+\frac{1}{2}}^{-1} \left(U_{i+\frac{1}{2}}^R - U_{i+\frac{1}{2}}^L \right) \quad (2.9)$$

where (\cdot) indicates evaluation at the Roe averaged state between U^L and U^R [9]. This scheme extends to second order accuracy through the MUSCL approach (Eqns. 2.5 and 2.6) and was applied in conjunction with the van Albada limiter [38, 8].

$$\hat{\Lambda}_{i+\frac{1}{2}} = \frac{\Delta_{i-\frac{1}{2}} \left[\left(\Delta_{i+\frac{1}{2}} \right)^2 + \delta_2 \right] + \Delta_{i+\frac{1}{2}} \left[\left(\Delta_{i-\frac{1}{2}} \right)^2 + \delta_2 \right]}{\Delta_{i+\frac{1}{2}}^2 + \Delta_{i-\frac{1}{2}}^2 + 2\delta_2} \quad (2.10)$$

where δ_2 is a small constant to prevent division by zero. In contrast to the above flux vector split algorithms, Roe's scheme may violate the entropy condition when the eigenvalues at the Roe averaged state vanish. Following Harten [39] the eigenvalues $|\lambda|$ of $|A|$ are modified when they are below some small threshold δ :

$$|\lambda| = \frac{|\lambda^2 + \delta^2|}{2\delta} \quad |\lambda| < \delta \quad (2.11)$$

Non-MUSCL Approach

The works of Yee [34] and Harten and Yee [36] provide two popular examples of non-MUSCL upwind schemes. The first order formulations of both reduce identically to the Roe solver.

- Yee's "Symmetric" TVD scheme [34, 35]:

This method takes the following form:

$$F_{i+\frac{1}{2}} = \frac{1}{2} (F(U_{i+1}) + F(U_i)) + \frac{1}{2} \hat{R}_{i+\frac{1}{2}} \Phi_{i+\frac{1}{2}} \quad (2.12)$$

where $\phi_{i+\frac{1}{2}}^l$ is the l^{th} component of Φ given by:

$$\phi_{i+\frac{1}{2}}^l = -|\hat{\lambda}_{i+\frac{1}{2}}^l| \left[\alpha_{i+\frac{1}{2}}^l - Q_{i+\frac{1}{2}}^l \right] \quad (2.13)$$

Here again $|\lambda|$ is thresholded as in the Roe scheme (Eqn. 2.11). Also:

$$\alpha_{i+\frac{1}{2}}^l = \hat{R}_{i+\frac{1}{2}}^{-1} (U_{i+1} - U_i) \quad (2.14)$$

is essentially the difference of the characteristic variables and $Q_{i+\frac{1}{2}}^l$ is the limiter taken from [8] (Eqn 3.51h).

$$Q_{i+\frac{1}{2}}^l = \text{minmod} \left[2\alpha_{i-\frac{1}{2}}^l, 2\alpha_{i+\frac{1}{2}}^l, \frac{1}{2} \left(\alpha_{i-\frac{1}{2}}^l + \alpha_{i+\frac{1}{2}}^l \right) \right] \quad (2.15)$$

It is the addition of this limiter which brings the scheme to second order. Setting $Q^l = 0$ reduces this method identically to Roe's first order scheme.

• **Harten and Yee's "Upwind" TVD Scheme [36, 35]:**

The modified flux approach of Harten and the modifications by Harten and Yee provide an alternative second order approach. This may be couched in the form of Eqn. 2.12 by redefining Φ for the l^{th} component.

$$\phi_{i+\frac{1}{2}}^l = \frac{1}{2} \psi \left(\hat{\lambda}_{i+\frac{1}{2}}^l \right) (g_{i+1}^l + g_i^l) - \psi \left(\hat{\lambda}_{i+\frac{1}{2}}^l + \gamma_{i+\frac{1}{2}}^l \right) \alpha_{i+\frac{1}{2}}^l \quad (2.16)$$

where:

$$\gamma_{i+\frac{1}{2}}^l = \frac{1}{2} \psi \left(\hat{\lambda}_{i+\frac{1}{2}}^l \right) \begin{cases} \frac{(g_{i+1}^l - g_i^l)}{\alpha_{i+\frac{1}{2}}^l} & \text{if } \alpha_{i+\frac{1}{2}}^l \neq 0 \\ 0 & \text{if } \alpha_{i+\frac{1}{2}}^l = 0 \end{cases} \quad (2.17)$$

and ψ enforces the entropy condition by preventing $|z|$ from reaching zero.

$$\psi(z) = \begin{cases} |z| & |z| \geq \delta \\ \frac{(z^2 + \delta^2)}{2\delta} & |z| < \delta \end{cases} \quad (2.18)$$

The limiter function g is taken from [8] (Eqn. 3.51f).

$$g_i^l = \frac{\alpha_{i-\frac{1}{2}}^l \alpha_{i+\frac{1}{2}}^l + \left| \alpha_{i-\frac{1}{2}}^l \alpha_{i+\frac{1}{2}}^l \right|}{\alpha_{i-\frac{1}{2}}^l + \alpha_{i+\frac{1}{2}}^l + \delta_2} \quad (2.19)$$

The three previous methods (Roe flux difference splitting, Symmetric and Upwind TVD) are implemented in a cell vertex finite volume formulation [40].

Central Difference Schemes

To provide a datum by which to evaluate the upwind procedures, the comparison includes formulations of two popular centered schemes.

- Jameson's classical five-point scheme [31] with second and fourth order artificial dissipation implemented in a node based manner [40].
- Ni's nine-point finite volume formulation of the classical Lax-Wendroff procedure [32] with the addition of second and fourth order dissipation [41].

Three distinct time integration techniques are utilized in this research. The Steger-Warming and van Leer flux split schemes are integrated in time using the implicit Gauss-Seidel line relaxation algorithm described by MacCormack [33]. Following the conclusions of Liou and van Leer [18], the implicit operator utilizes the Steger-Warming Jacobians for both splittings. With the exception of the Lax-Wendroff scheme, all other schemes use explicit multistage Runge-Kutta algorithms. Table 1.1 highlights the schemes and numbers them for discussion in later sections.

3. Overview and Classification of Computations

In order to assess the quality of the current implementation of each scheme for high speed flow, some basic issues are examined on a simple problem. A noninterfering 2-D cylinder (Case A) at Mach 8.03 provided a qualitative check of the convergence properties and the shock stand off distances obtained by each scheme. This case also brought to light the behavior of the sonic line in view of the limiting characteristic theory provided in classical references [42].

This simple problem gives some preliminary insight into the shock capturing capability and overall accuracy of the various schemes. The shock capturing capability is investigated by line plots across grid-aligned and nonaligned portions of the bow shock. Shock resolution is also examined as a function of Mach number with the addition of a Mach 16.33 noninterfering cylinder. In addition, a grid refinement study on stagnation enthalpy losses along a streamline at Mach 8.03 provides an indication of the net error in each scheme.

With results of these basic investigations in mind, the discussion turns to the complex shock-shock interaction mentioned earlier. This problem (Case B) results in severe mechanical and thermal gradients throughout the field and on the boundary. In the sketch of Figure 1, the terminating normal shock results in surface pressures which exceed the non-impinging case by an order of magnitude. Numerically, this case focuses attention on scheme performance in complex flows. Moreover, since the geometry remains simple, this complexity stems from shock and slip line structure within the flow field, rather than from an arbitrary boundary geometry. This structure gives rise to many interdependent time scales which require many characteristic times to pass before a steady state establishes itself. In an effort to add rigor to this comparison, the Type IV problem is investigated on a series of three successively refined meshes. All flow and grid parameters are listed in Table 3.1.

Case	Mach Number	Grids ($IL \times JL$)	Flow
A	8.03,16.33	$20 \times 20, 40 \times 40$	Noninterfering
B	8.03	$60 \times 40, 120 \times 80, 240 \times 160$	Interfering (Type IV)

Table 3.1: Classification of computations for flow past a 2-D cylinder

3.1 Criteria for Comparison

Throughout this effort, emphasis was placed on proper comparison of the various algorithms. At each level of refinement and for each problem, all calculations were completed on the same computational meshes. Furthermore, identical convergence criteria were applied to each of the algorithms.

These criteria include root mean square (RMS) measures of the global residual of all conserved variables as well as integrated surface pressure.

- Global residual:

$$\|G.R.\| = \frac{1}{(IL)(JL)} \sqrt{\sum_{i=1}^{IL} \sum_{j=1}^{JL} \sum_{k=1}^4 \left(\frac{R_k}{U_\infty} \right)^2} \quad (3.1)$$

where k denotes the k th equation on an $IL \times JL$ computational mesh and R_k is the residual:

$$R_k \cong \frac{\partial U_k}{\partial t} = -\frac{\partial F_k}{\partial x} - \frac{\partial G_k}{\partial y} \quad (3.2)$$

For plotting purposes, these values are normalized by the value of $\|G.R.\|$ obtained after the first iteration.

- RMS Surface pressure:

$$\left\| \frac{p}{p_\infty} \right\| = \frac{1}{IL} \sqrt{\sum_{i=1}^{IL} \left(\frac{P_{i,j=surface}}{P_\infty} \right)^2} \quad (3.3)$$

Both residuals are plotted against the characteristic time $T_c = L/V_\infty$ where L is a characteristic length scale (chosen as the cylinder diameter) and V_∞ is the freestream velocity of the incoming flow upstream of the impinging shock. T_c provides a uniform global time scale for comparison of all methods.

4. Results

4.0.1 Case A - Blunt Body

Figure 2 displays the convergence behavior of the seven schemes for Mach 8.03 flow past a 2-D cylinder. The calculations progressed until the residuals dropped five orders of magnitude. In this calculation, as throughout this research, no emphasis was placed on efficiency. Clearly, by adjusting some parameter, convergence of any of these schemes could be accelerated. This figure is intended only to demonstrate that all schemes converge for this problem and provides a basis for the investigations which follow.

Figure 3 exhibits the RMS surface pressure for each scheme. With this criterion, all schemes converge within one characteristic time and the discrepancy in asymptotic levels may be ascribed to slight differences in normalization and are considered unimportant.

Figure 4 shows both the 40×40 mesh and Mach contours for each of the seven schemes. Mach contours are drawn in increments of 0.25 and the 1.0 contour (sonic line) is annotated in each plot. In all cases, the sonic line displays the highly curved profile associated with 2-D flows above Mach 2. Additionally, the stand-off distance in all cases agrees with the value published in classical texts [42] to within a grid point (measured from the "first shock point" away from the body).

While the contour plots give some indication of the scheme's ability to capture strong shocks, a more precise examination stems from line plots of Mach number along specific radial mesh lines. Figure 5 contains such a plot along the stagnation streamline while Figure 6 contains the same plot for a ray inclined 36° degrees from the vertical. These plots clearly demonstrate the superior shock resolution of the upwind schemes as compared to the centered methods. Moreover, they also show the nonoscillatory nature of the flux limited upwind schemes.

Figures 7 and 8 show the same line plot for a Mach 16.33 calculation on the same grid. While the central difference schemes each require at least one additional grid point in the shock, the upwind schemes still resolve the shock with only two intermediate cells. Of particular note are

the crisp shocks afforded by the schemes of Roe, van Leer and Upwind TVD. The relatively poor performance of the Ni scheme off-centerline at this Mach number (Fig. 8) may be ascribed to the use of the diagonals in the difference stencil – in contrast to the other schemes which excludes these nodes (e.g., [40]).

Figure 9 displays the stagnation enthalpy losses along the stagnation streamline. Following the upwind schemes (3 through 7) along this streamline, perturbations appear within the discrete shock and all curves exit with slightly different (negative) values. Through the shock, all the flux limited schemes reduce their approximation of the governing equations to first order as the limiter “clips off” the solutions at extrema. This is responsible for the stagnation enthalpy error immediately following the shock. It is worth noting that this post-shock error decreases for all schemes with grid refinement. After the shock, the methods again become second order, but despite this, only the van Leer and Roe schemes remain reasonably constant on either grid. Of the other upwind schemes, only the Steger-Warming algorithm is of particular note as its extreme diffusivity creates an error of over 10% on both grids. In evaluating any particular method, both its overall and post-shock behavior must be considered. Of the current implementations, the van Leer algorithm shows the least discrepancy along the stagnation streamline. The Jameson central difference scheme (scheme 1) exhibits a large stagnation enthalpy drop across the shock due to the large second order damping required to capture the strong Mach 8.03 normal shock. In the subsonic post-shock region, however, considerable improvement is observed with grid refinement as the method demonstrates its well known ability to solve subsonic flows [43].

4.0.2 Case B - Type IV Interference Flow

The next set of figures presents results for the shock interaction test case at Mach 8.03 on a 60×40 grid. Figure 1 presents details of the geometry and parameters specifying this problem. Figures 10 and 11 display the global residual and surface pressure convergence histories for all the methods. These plots display converged results only for schemes 3, 5, and 6 and while the van Leer and Upwind TVD methods exhibit declining residuals, convergence cannot be conclusively

claimed. However, the surface pressure (Figure 11) indicates a solution converged to plotting accuracy. Both central difference schemes appear to level off after dropping about two orders of magnitude and show small, high frequency perturbations around a constant value. However, these oscillations are small enough that no changes in the flow field are observed. These schemes required a second difference smoothing coefficient about 1.5 times that needed in the blunt body calculation, and could only be run at a CFL number more than 10 times smaller than in the noninterfering case. Notice that since some experimental and computational evidence exists which suggests an unsteady solution all schemes were run with a constant global timestep [23, 30, 25].

Figure 12 compares contours of constant Mach number for the schemes under investigation. These contours have an increment of 0.25 and are labeled in the last frame. This figure also contains a plot of the coarse computational mesh (which was not optimized excessively for this problem). Proper resolution of this interaction demands both accurate representation of strong shocks and shear layers throughout the interference pattern within the distorted bow shock.

As anticipated, the additional dissipation required to curtail oscillations in the centered scheme's convergence history, considerably smears both the impinging shock and the distorted bow shock. All the upwind methods resolve these two features with roughly the same resolution. The dissipative nature of the upwind schemes is most evident in the Steger-Warming splitting. Here, the internal structure of the field is smeared even more than with the central schemes, and the contours are uniformly smooth throughout the field. Of the four schemes (4 through 7) which capture the embedded shock and terminating normal shock, the van Leer, Roe and Upwind TVD methods perform perceptibly better than the Symmetric TVD scheme. All four algorithms predict supersonic jets of comparable width.

The final figure for the coarse grid Type IV calculation presents normalized surface pressure as a function of θ (see Fig. 1). In Figure 14, the vertical axis is normalized by the stagnation pressure behind a Mach 8.03 normal shock (to show *pressure amplification*). Here, results from the seven calculations are compared with results from the experiment by Wieting and Holden [29]. Away from the peak, all schemes agree reasonably well with the available data. Each of the schemes places the peak at roughly the same angular location, but are also shifted about 3° from the

experimentally observed peak. Since the angular location of the peak is a strong function of the impinging shock location, this small discrepancy is not considered important for the purposes of the present investigation. The Steger-Warming method underpredicts the maximum pressure augmentation considerably. Supporting the similarities shown in the contour plots of the previous figure, the Roe flux difference splitting and the Upwind TVD schemes remain nearly inseparable on this plot, achieving a value somewhat higher than the Symmetric TVD scheme. The van Leer splitting reaches a slightly higher peak but is shifted roughly 2° to the right of the others. Despite the apparent lack of structure in the contour plots for the central difference schemes, both predict very reasonable values for the peak over pressure.

In an effort to bring schemes 1, 2, 4 and 7 closer to convergence, the solutions were marched out several more characteristic times. With this, both the van Leer and Upwind TVD algorithms converged fully. However, no reasonable combination of second and fourth difference dissipation coefficients could be found to fully lead the central difference schemes to convergence. Over the course of this search, the peak surface pressure varied from 6 to 8.5 and the "loop" structure (evident in the solution of schemes 4 through 7 of Figure 12) occasionally became evident. However, at damping coefficients lower than those reported during the discussion of Figure 12, the high frequency oscillations shown in the convergence plots increased in amplitude. Figure 13 shows the surface pressure history of the Lax-Wendroff scheme with a second difference smoothing coefficient equal to that of the blunt body case. This figure shows a small high frequency oscillation superimposed on a large periodicity which spans about 10 characteristic times. This plot also shows the structure of the flow field at two different locations in the pressure cycle. Note that this period corresponds to a physical frequency of 2200 Hz which is slightly lower than the range (3 kHz-10 kHz) reported by Holden *et al.* [23].

The fact that this unsteady behavior increased as diffusion was removed from the solutions led to questions about the diffusion present in the discrete solutions of the upwind schemes. Returning briefly to Figure 12 permits a crude estimation of the relative diffusivity in the upwinded discrete solutions. The smooth, rounded contours of the Steger-Warming solution are indicative of excess dissipation which makes itself evident in the underprediction of the pressure peak in Figure 14.

The contours in the Upwind TVD and Roe flux difference splitting schemes exhibit nearly identical smoothness which correlates well with the similarity in their pressure peaks. The van Leer result, however, demonstrates that this value cannot be exclusively linked to the diffusion in the field. Despite the fact that its subsonic contours are somewhat smoother than schemes 5 or 7, the pressure peak is the highest of all the upwind algorithms.

In an effort to make a more quantitative estimate of the diffusivity of the various upwind methods in this complex flow, the truncation error in the solution was reduced by refining the mesh. Figures 15 and 16 contain the global residual and surface pressure convergence histories for one of the central methods (Scheme 1) and all the upwind algorithms on a 120×80 mesh. On this finer mesh, only the convergence behavior of the two flux vector split schemes remains unaltered. Nevertheless, the surface pressure history of the Symmetric TVD scheme appears to be quite steady. Again, all these calculations maintained a constant global timestep in an attempt at time accuracy. Moreover, marching the solution out several characteristic times did not alter these trends significantly.

Since the two implicitly integrated flux vector split schemes (3 and 4) were the only ones to converge on this grid, the effect of the time integration scheme was investigated in further detail. The van Leer splitting was reapplied to the problem using a second order time-accurate explicit predictor-corrector algorithm on both meshes. Both convergence criteria were unaffected on the coarse mesh (Fig. 17). On the medium grid, however, the pressure residual remained unchanged but the global residual with the explicit integration dropped only two orders of magnitude and then remained generally steady – albeit with small amplitude high frequency oscillations. No difference in surface pressure or flow structure could be observed at these levels.

Figure 18 displays the contour plots of constant Mach number on the 120×80 mesh. Of course, the detailed structure in the plots for the oscillatory behaved solution is a function of the current characteristic time. Nevertheless, all the plots presented are representative pictures of the solution provided by each scheme. All the methods show increased resolution as compared to the coarse grid plots of Figure 12. On this medium grid, both the Jameson and Steger-Warming schemes show the loop structure demonstrated by the other upwind schemes on the coarse grid. Despite

the accurate shocks evident in the Steger-Warming calculation, the internal structure is less apparent than in the central difference solution. Again, methods 4 through 7 demonstrate superior resolution in these plots. As on the coarse mesh, the van Leer and Symmetric TVD methods give very similar looking results. After passing through the terminating normal shock, most of the flow accelerates and expands upward around the body. This flow forms a supersonic/subsonic shear layer with the nearly stagnated flow behind the bow shock. Both the Roe and Upwind TVD methods appear to show a developing shock reflection system within this shear layer.

Figure 19 presents a detailed view of a typical result (Upwind TVD) through velocity vectors. Figure 20 shows a few representative particle traces (PLOT3D) superimposed on selected Mach contours. The streamlines detail the flow's progress through the interference and stagnation regions of the flow field.

Figure 21 contains a plot of normalized surface pressure for the methods on the medium grid. Note again that the unsteady result for the Roe flux difference splitting and Upwind TVD methods are shown as "snapshots" taken at the same characteristic time as the contours in Figure 18. Qualitatively, all the peaks on this plot are higher than on the coarse grid.

As a further investigation of the oscillatory behavior demonstrated by the Upwind TVD and Roe flux difference split schemes, Figures 22 and 23 present the solution of the Upwind TVD algorithm at extrema in the solution cycle. Both low and high frequency oscillations appear in the surface pressure convergence behavior. The convergence history is reproduced on both figures for the solution between 90 and 120 characteristic times. While there is little evidence of the low frequency oscillations in the Mach and surface pressure distributions, the high frequency oscillation has dramatic effects on both. The unsteadiness manifests itself through changes in the angle of the terminating normal shock, which in turn influences the angle at which the jet impinges on the surface. This sets up different oblique shock reflection patterns within the supersonic layer bounded by the sub/supersonic shear layer and the body. Looking more closely at Figures 22 and 23, the higher peaks in the surface pressure plot correspond to the pattern where the jet terminating normal shock is more closely aligned with the body surface. Returning to the solution with the van Leer scheme on this grid (Figures 18 and 21), both the terminating shock angle and

the surface pressure distribution with this method correspond very closely to the Upwind TVD solution at the maximum point in the oscillation of the RMS surface pressure distribution.

Although the van Leer and Symmetric TVD schemes provided reasonably accurate surface pressure distributions (Figure 21), they fail to resolve the reflected shock structure within the supersonic region bounded by the upper body and the sonic line (Figure 18) seen in the discrete solutions of Roe and Upwind TVD. Moreover, neither method predicted an unsteady flow solution. With the intent of resolving more structure within the supersonic layer and to further investigate the convergence behavior of the van Leer and Symmetric TVD schemes, the truncation error was reduced further by again refining the mesh. These two schemes were applied to a mesh constructed by doubling the number of points in each coordinate direction (resulting in a 240×160 mesh).

Figures 24 and 25 present convergence behavior and Mach contour distributions for the van Leer and Symmetric TVD discrete solutions on the fine grid. In Figure 24 the upper frame chronicles the global residual variation for 50 characteristic times. As anticipated, both schemes now predict unsteady behavior with high frequency oscillations as seen earlier in Roe and Upwind TVD solutions on the medium grid (Figures 15 and 16). The lower frame records RMS surface pressure over the same period of time. The smaller amplitude of the oscillations of the van Leer scheme correspond to the lower magnitude of its residual in the upper frame of this figure. In Figure 25, both these schemes now capture the reflected shock structure within the supersonic layer flowing up over the body surface as seen on the medium grid with the Roe and Upwind TVD methods. With reduced truncation error present on the fine grid, both solutions are now unsteady and, as a result, slight differences may be expected between the two plots despite higher order time accuracy.

Figure 26 presents a schematic of the flow structures evidenced by the discrete solutions in Figures 18, 22 and 25. This schematic identifies the supersonic flow region bounded by the body and the sub/supersonic shear layer which forms around the upper surface of the body. The picture suggests a possible feedback mechanism which may be responsible for the unsteadiness in the oblique shock reflection patterns shown in Figure 22. With the terminating normal shock at some initial angle, an associated oblique shock pattern will establish itself between the shear layer

and the body. As these oblique shocks form, they disturb this shear layer, communicating these disturbances to the subsonic region. Within the subsonic stagnation region, these disturbances are free to propagate in all directions including back toward the upper shear layer (see Fig. 1). As these waves distort the interaction region, they may change the angle of the terminating normal shock setting up a new oblique shock reflection system which again distorts the subsonic shear layer thus reinitiating the cycle. While this hypothesis seems reasonable and physical, it does not satisfactorily explain the difference in frequency between the computed and experimental results.

5. Conclusion

A comparative study has been performed for a variety of upwind schemes applied to a problem of realistic complexity. The schemes which achieve second order accuracy through the MUSCL approach included the Steger Warming and van Leer flux vector split schemes and the Roe flux difference split scheme. Additionally, this comparison investigated two non-MUSCL algorithms based on the "Symmetric" and "Upwind" TVD methods of Yee and Harten and Yee.

The shock capturing ability of the upwind schemes was demonstrated for grid aligned and nonaligned shocks at two different Mach numbers. This investigation clearly showed the superior shock resolution afforded by these procedures. Moreover, this ability was found to be independent of Mach number, which is not the case for central schemes.

The Type IV shock interference flow pointed out differences among the upwind procedures. In particular, the extreme diffusivity of the Steger-Warming method – which was not immediately evident in the blunt body solutions – became apparent and unacceptably corrupted the solution. The other four upwind procedures all captured considerable flow field detail with a slight advantage falling to the Upwind TVD and Roe's algorithm.

A comparison of flow structure on a successively refined sequence of three meshes indicated the least diffusion in the Upwind TVD and Roe flux difference split discrete solutions. These two schemes already showed oscillatory behavior on a 120×80 grid. The Symmetric TVD and van Leer algorithms also led to oscillatory flows for this problem but required an even finer mesh (240×160) to demonstrate this behavior.

Despite the apparent lack of structure within the flow solution caused by the inability of the central difference algorithms to resolve features on the order of the mesh scale, both these schemes provided reasonable surface pressure distributions. Moreover, these procedures demonstrated neutral convergence behavior on the coarse grid. Although such behavior became apparent in some upwind procedures on finer meshes, it is not clear that the same mechanism is responsible for the unsteadiness observed in the central and upwind solutions.

6. References

- [1] A. Jameson and T.J. Baker, "Solution of the Euler Equations for Complex Configurations," *AIAA Paper 83-1929*, 1983.
- [2] G. Volpe and A. Jameson, "An Efficient Method for Computing Transonic and Supersonic Flows About Aircraft," *ICAS-88-4.8.3*, 1988.
- [3] N. Kroll, C. Rossow, S. Scherr, J. Schone, and G. Wichmann, "Analysis of 3-D Aerospace Configurations Using the Euler Equations," *AIAA Paper 89-0268*, 1989.
- [4] C. Koeck, "Computation of Three-Dimensional Flow Using the Euler Equations and a Multiple Grid Scheme," *Int. Journal for Numerical Methods in Fluids*, 5:483-500, 1985.
- [5] G. Huband, J. Shang, and M. Aftosmis, "Numerical Simulation of an F-16A at Angle of Attack," *AIAA Paper 90-0100*, 1990.
- [6] P.L. Roe, "A Survey of Upwind Differencing Techniques," In *Proceedings of the 11th International Conference on Numerical Methods in Fluid Dynamics*, 1988.
- [7] M. Pandolfi, "On the "Flux-Difference" Splitting Formulation," In *Proceedings of the 2nd International Conference on Hyperbolic Problems, Aachen, West Germany*, 1988.
- [8] H.C. Yee, "A Class of High-Resolution Explicit and Implicit Shock-Capturing Methods," *von Karman Institute for Fluid Dynamics, Lecture Series 1989-04*, 1989.
- [9] P.L. Roe, "Approximate Riemann Solvers, Parameter Vectors and Difference Schemes," *Journal of Computational Physics*, 43:357-372, 1981.
- [10] S. Chakravarthy and S. Osher, "A New Class of High Accuracy TVD Schemes for Hyperbolic Conservation Laws," *AIAA Paper 85-0363*, 1985.
- [11] B. van Leer, "Flux-Vector Splitting For the Euler Equations," Technical Report 82-30, ICASE, September 1982.

- [12] J.L. Steger and R.F. Warming, "Flux Vector Splitting of the Inviscid Gasdynamic Equations with Application to Finite Difference Methods," *Journal of Computational Physics*, 40(2):263-293, April 1981.
- [13] W.K. Anderson, J.L. Thomas, and B. van Leer, "A Comparison of Finite Volume Flux Vector Splittings for the Euler Equations," *AIAA Paper 85-0122*, 1985.
- [14] A. Harten, "On a Class of High Resolution Total-Variation-Stable Finite-Difference Schemes," *SIAM Journal of Numerical Analysis*, 21:1-23, 1984.
- [15] H.C. Yee, G.H. Klopfer, and J.-L. Montagne, "High-Resolution Shock-Capturing Schemes for Inviscid and Viscous Hypersonic Flows," Technical Report 100097, NASA - Ames Research Center, Moffet Field, California, April 1988.
- [16] D.P. Rizzetta and K.D. Mach, "Comparative Numerical Study of Hypersonic Compression Ramp Flows," *AIAA Paper 89-1877*, 1989.
- [17] B. van Leer, J.L. Thomas, P.L. Roe, and R.W. Newsome, "A Comparison of Numerical Flux Formulas for the Euler and Navier-Stokes Equations," *AIAA Paper 87-1104*, 1987.
- [18] M-S. Liou and B. van Leer, "Choice of Implicit and Explicit Operators For the Upwind Differencing Method," *AIAA Paper 88-0624*, 1988.
- [19] P. Buelow, "Comparison of TVD Schemes Applied to the Navier-Stokes Equations," *AIAA Paper 89-0847*, 1989.
- [20] S-H. Chang and M-S. Liou, "A Numerical Study of ENO and TVD Schemes for Shock Capturing Schemes," Technical Report 101355, NASA-TM, September 1988.
- [21] J-L. Montagne, H.C. Yee, and M. Vinokur, "Comparative Study of High Resolution Shock-Capturing Schemes for a Real Gas," Technical Report 100004, NASA-TM, July 1987.

- [22] B. Grossman, P. Cinnella, and J. Garrett, "A Survey of Upwind Methods for Flows with Equilibrium and Non-Equilibrium Chemistry and Thermodynamics," *AIAA Paper 89-1653*, 1989.
- [23] M.S. Holden, A.R. Wieting, J.R. Moselle, and C. Glass, "Studies of Aero thermal Loads Generated in Regions of Shock/Shock Interaction in Hypersonic Flow," *AIAA Paper 88-0477*, 1988.
- [24] R.R. Thareja, J.R. Stewart, O. Hassan, K. Morgan, and J. Peraire, "A Point Implicit Unstructured Grid Solver for the Euler and Navier-Stokes Equations," *International Journal for Numerical Methods in Fluids*, 1989.
- [25] R.K. Prabhu, J.R. Stewart, and R.R. Thareja, "Shock Interference Studies on a Circular Cylinder at Mach 16," *AIAA Paper 90-0606*, 1990.
- [26] G.H. Klopfer and H.C. Yee, "Viscous Hypersonic Shock-On-Shock Interaction on Blunt Cowl Lips," *AIAA Paper 88-0233*, 1988.
- [27] Y.J. Moon and M. Holt, "Interaction of an Oblique Shock Wave with Turbulent Hypersonic Blunt Body Flows," *AIAA Paper 89-0272*, 1989.
- [28] B. Edney, "Anomalous Heat Transfer and Pressure Distributions on Blunt Bodies at Hypersonic Speeds in the Presence of an Impinging Shock," Technical Report 115, The Aeronautical Research Institute of Sweden, Stockholm, February 1968.
- [29] A.R. Wieting and M.S. Holden, "Experimental Study of Shock Wave Interference Heating on a Cylindrical Leading Edge at Mach 6 and 8," *AIAA Paper 87-1511*, 1987.
- [30] K.M. Peery and S.T. Imlay, "Blunt-Body Flow Simulations," *AIAA Paper 88-2904*, 1988.
- [31] A. Jameson, W. Schmidt, and E. Turkel, "Numerical Solutions of the Euler Equations by a Finite Volume Method Using Runge-Kutta Time Stepping Schemes," *AIAA Paper 81-1259*, 1981.

- [32] R.H. Ni, "A Multiple Grid Scheme for Solving the Euler Equations," *AIAA Journal*, 20:1565–1571, October 1981.
- [33] R. MacCormack, "Current Status of Numerical Solutions of the Navier-Stokes Equations," *AIAA Paper 85-0032*, 1985.
- [34] H.C. Yee, "Construction of Implicit and Explicit Symmetric TVD Schemes and Their Applications," *Journal of Computational Physics*, 68:151–179, 1987.
- [35] H.C. Yee, "Upwind and Symmetric Shock-Capturing Schemes," Technical Report 89464, NASA-TM, 1987.
- [36] H.C. Yee and A. Harten, "Implicit TVD Schemes for Hyperbolic Conservation Laws in Curvilinear Coordinates," *AIAA Journal*, 25:266–274, 1987.
- [37] G.V. Candler, "The Computation of Weakly Ionized Hypersonic Flows In Thermo-Chemical Nonequilibrium," PhD thesis, Stanford University, California, 1988.
- [38] G.D. van Albada, B. van Leer, and W.W. Roberts, "A Comparative Study of Computational Methods in Cosmic Gas Dynamics," *Astron. Astrophys.*, 108:76–84, 1982.
- [39] A. Harten, "High Resolution Schemes for Hyperbolic Conservation Laws," *Journal of Computational Physics*, 49:357–393, 1983.
- [40] N. Kroll and C. Rossow, "A High Resolution Cell Vertex Scheme for the Solution of the Two and Three Dimensional Euler Equation," In *12th International Conference on Numerical Methods in Fluid Dynamics*, 1990.
- [41] J.F. Dannenhoffer III, "Grid Adaptation for Complex Two-Dimensional Flows," Sc.D thesis, Massachusetts Institute of Technology, Cambridge, Massachusetts, 1987.
- [42] W. Hayes and R. Probstein, "Hypersonic Flow Theory, volume I," Academic Press, New York, 1959.

- [43] AGARD, "Test Cases for Steady Inviscid Flow Field Methods, AGARD-AR-211 edition, 1985."
- [44] D.H. Crawford, "A Graphical Method for the Investigation of Shock Interference Phenomena," *AIAA Journal*, 11(11):1590-1592, November 1973.

Nomenclature

a	local sound speed
A	flux Jacobian matrix ($\frac{\partial F}{\partial U}$)
f_1	van Leer mass flux function for subsonic flow
g	limiter function for "Upwind" TVD scheme
\vec{F}, \vec{G}	flux density vectors
$G.R.$	global residual
IL, JL	number of mesh points in each coordinate direction
L	characteristic length
M	Mach number
p	pressure
Q	numerical flux function in TVD schemes
R	gas constant, right eigenvector matrix, residual
t	nondimensional time
T	temperature
T_c	characteristic time
u, v	Cartesian velocity components
\vec{U}	vector of conserved variables
V	magnitude of total velocity vector
x, y	two-dimensional Cartesian coordinates
α	difference in characteristic variables
δ	small constant $\delta \ll 1$
Δ	difference between left and right states
$\tilde{\Delta}$	limiter function for MUSCL type schemes

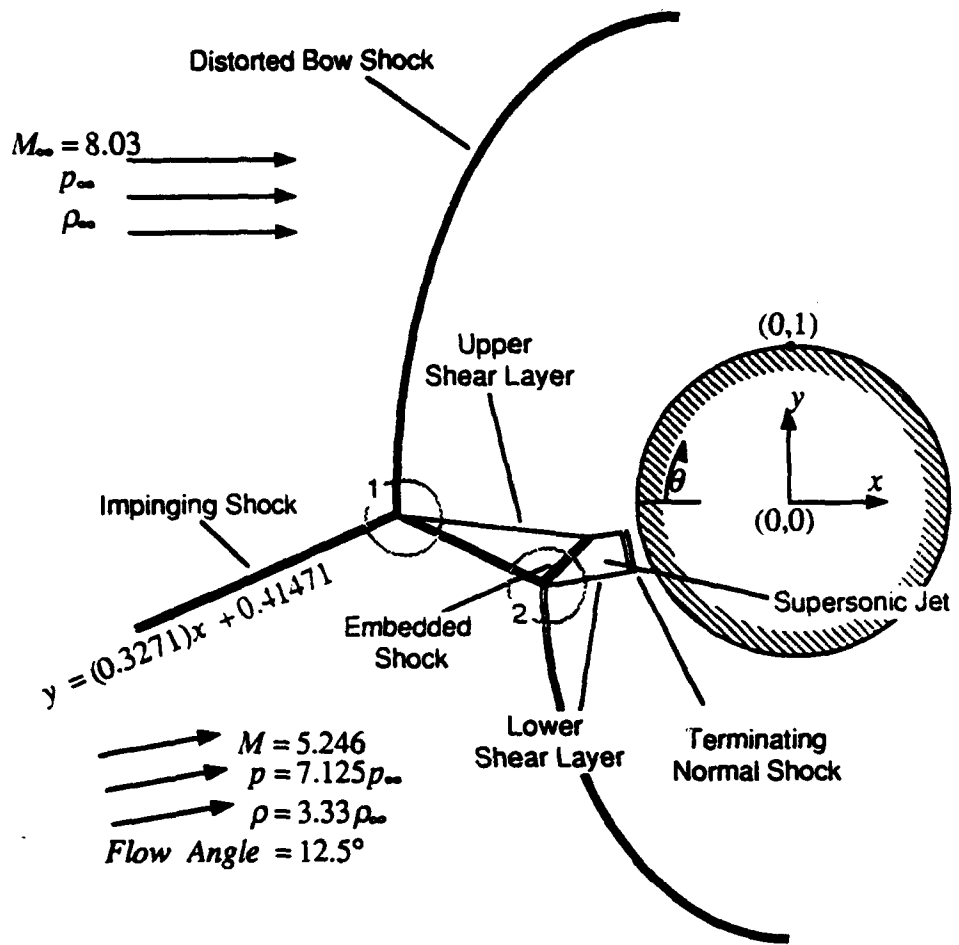
γ	ratio of specific heats
λ	eigenvalue
Λ	eigenvalue matrix
ϕ	element of Φ
Φ	limited flux function in TVD schemes
θ	circumferential angle
ρ	density
ψ	function enforcing entropy condition

Subscript

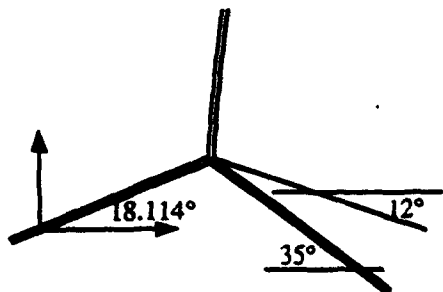
$(\)_{i+\frac{1}{2}}$	face to the right of i th node
$(\)_x$	x direction
$(\)_\infty$	freestream value

Superscript

$(\)^l$	l th component of vector
$(\)^L$	state to left of current face
$(\)^R$	state to right of current face
$(\)^{+,-}$	positive and negative components
$(\)^Roe$	Roe averaged state



Region 1



Region 2

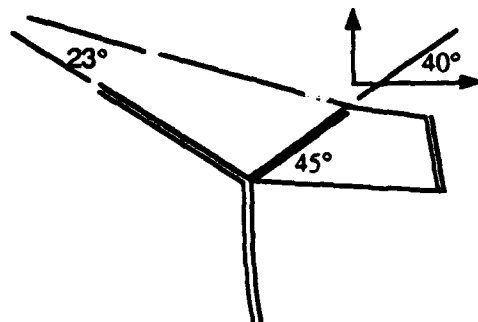


Figure 1: Schematic of Type IV shock-shock interaction of Edney [28]. Angles of shocks and shear layers calculated from oblique shock relations and hodograph methods of [44].

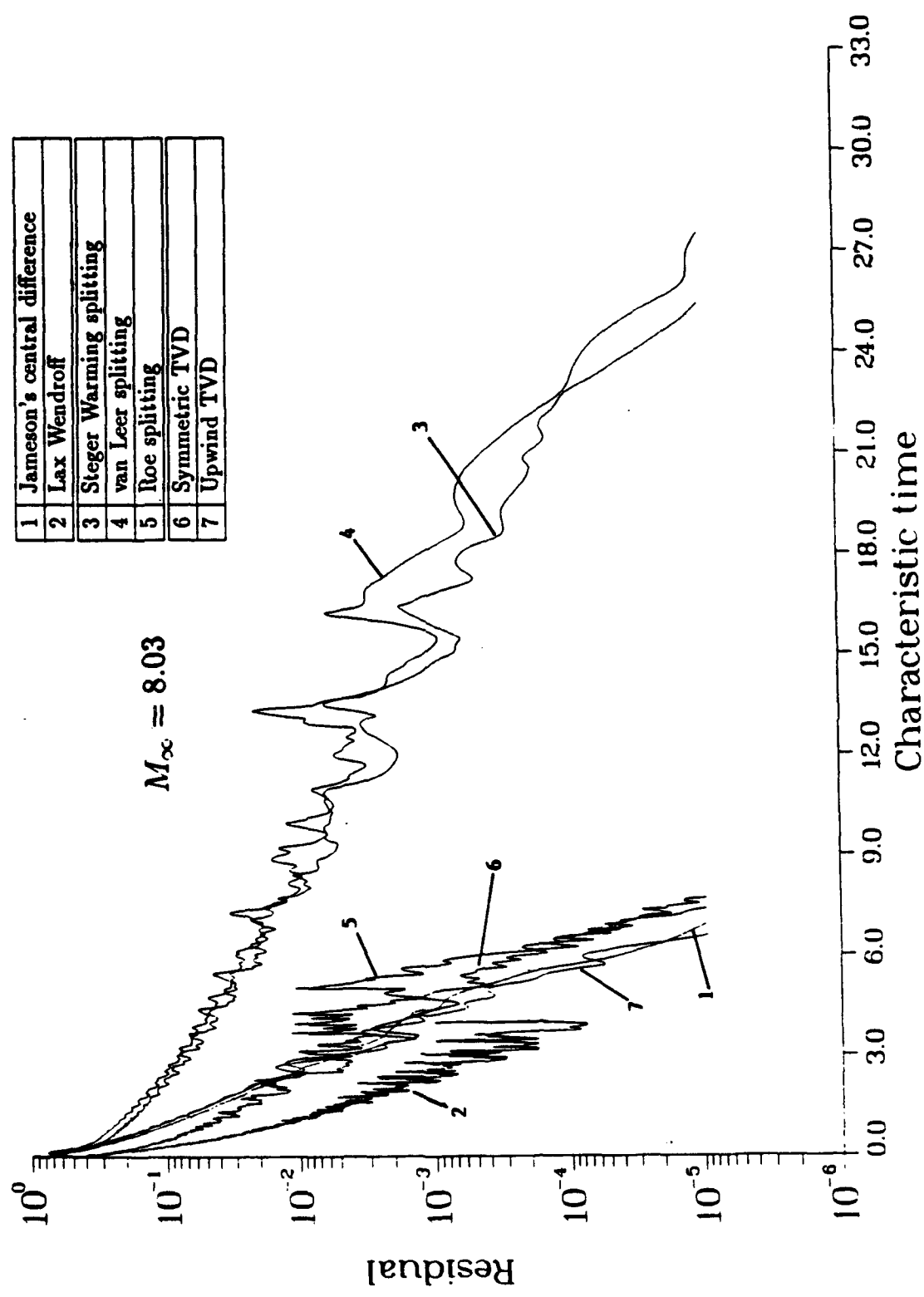


Figure 2: Residual convergence behavior for a blunt body on a 40x40 grid at Mach 8.03.

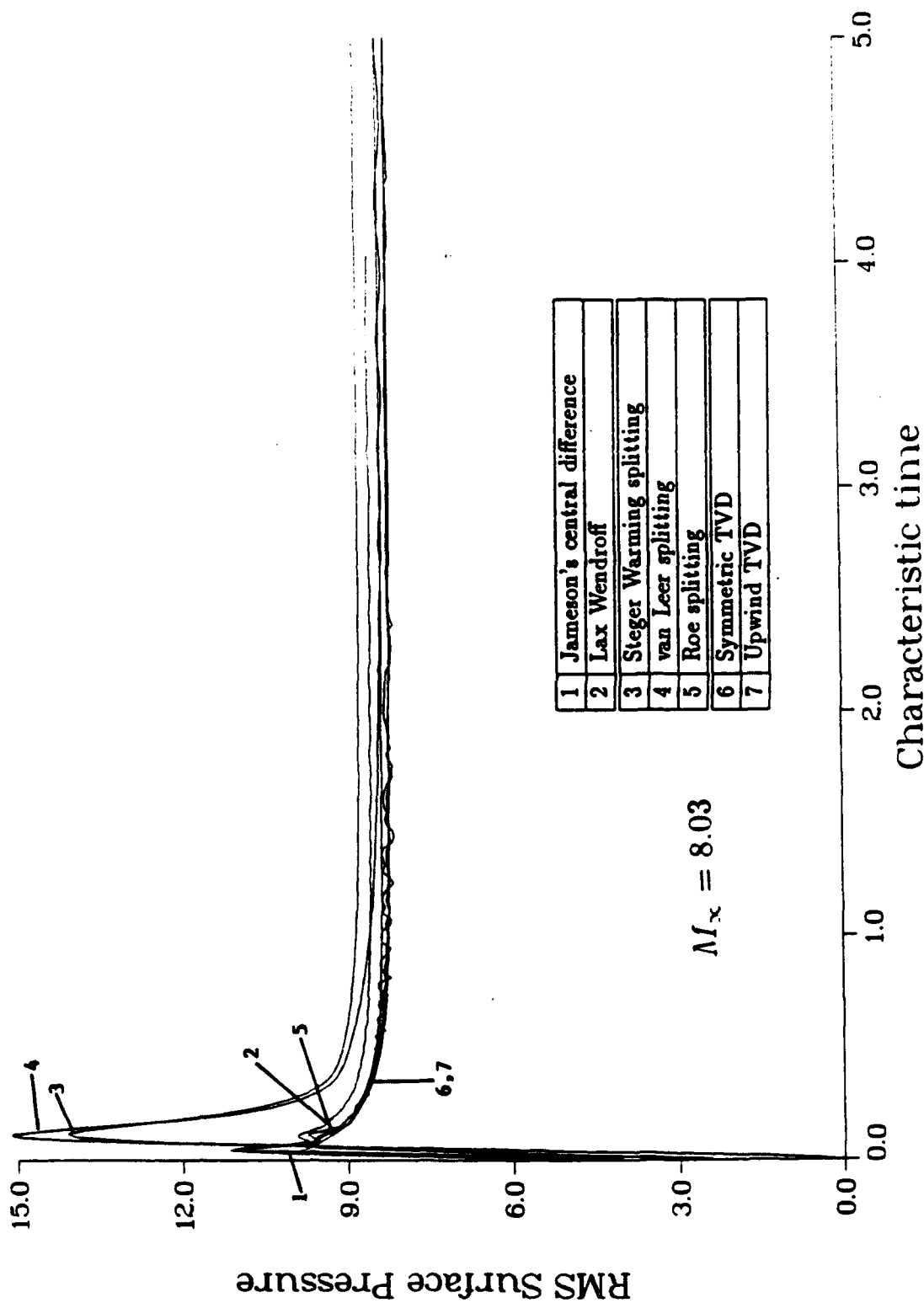


Figure 3: RMS surface pressure behavior for a blunt body on a 40x40 grid at Mach 8.03.

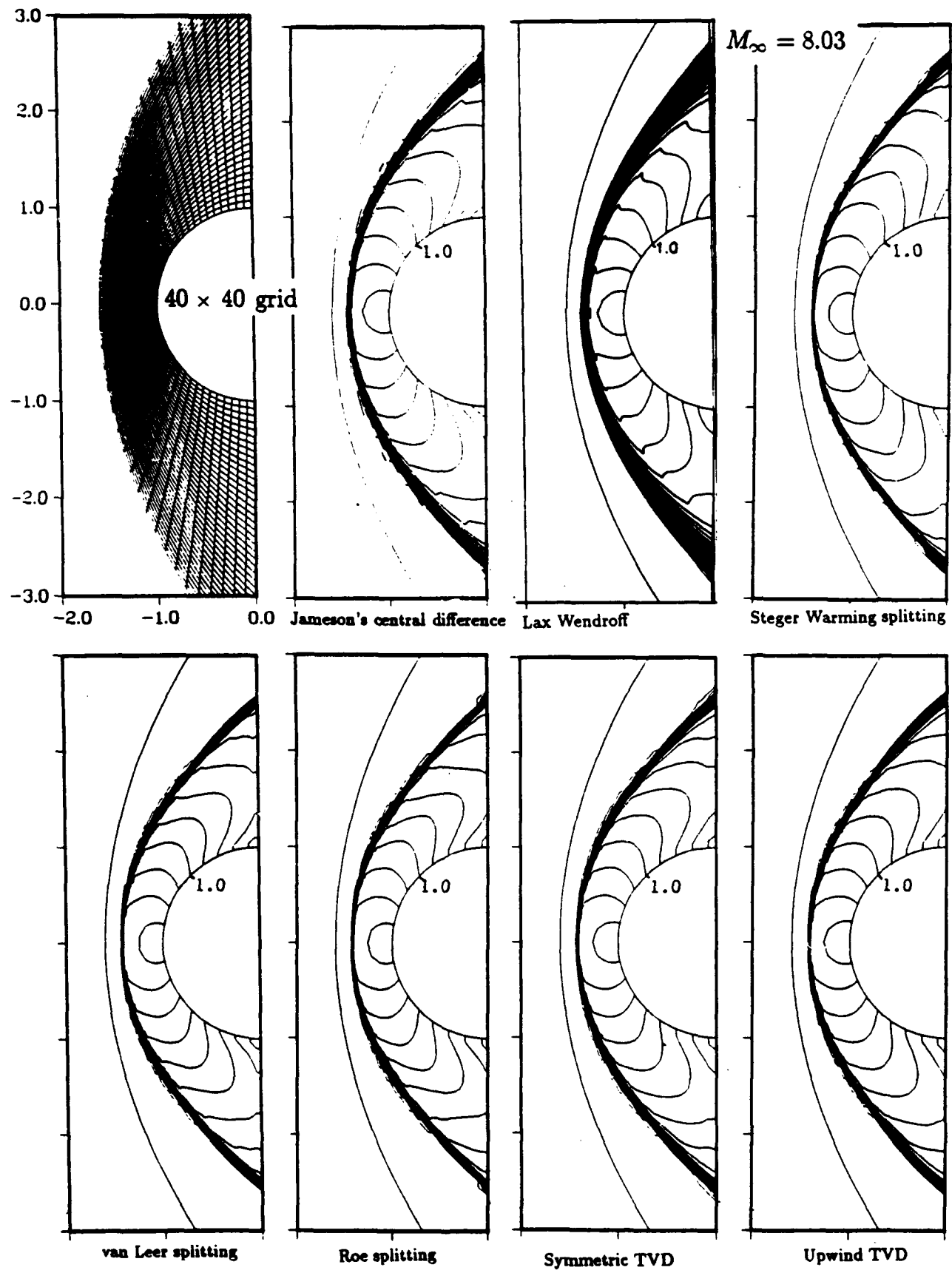


Figure 4: Mach contours for blunt body on a 40×40 grid at $Mach 8.03$.

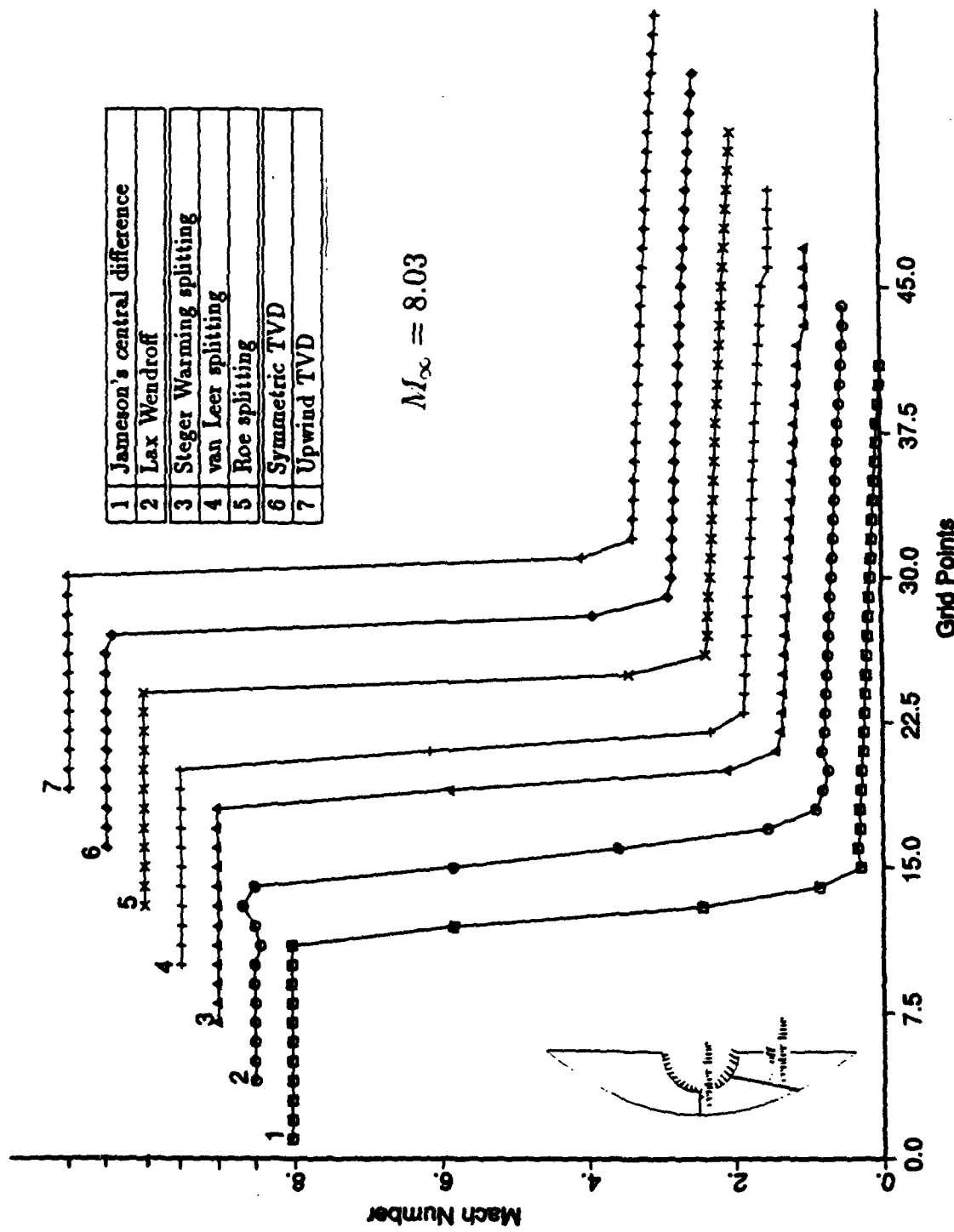


Figure 5: Mach number vs. grid point for a blunt body on a 40×40 grid at Mach 8.03 along the centerline.

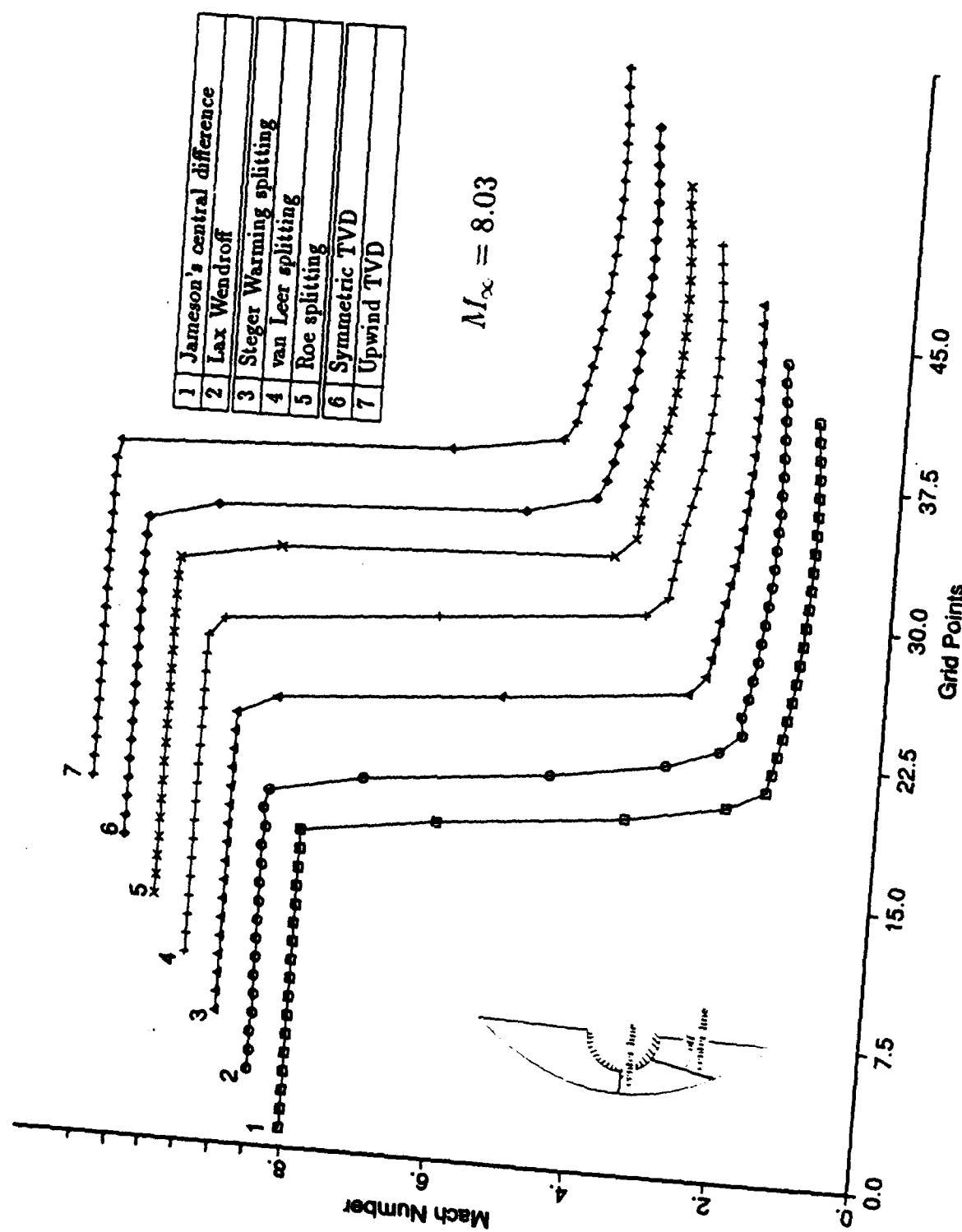


Figure 6: Mach number vs. grid point for a blunt body on a 40×40 grid at Mach 8.03 along a ray inclined at 36° to the vertical.

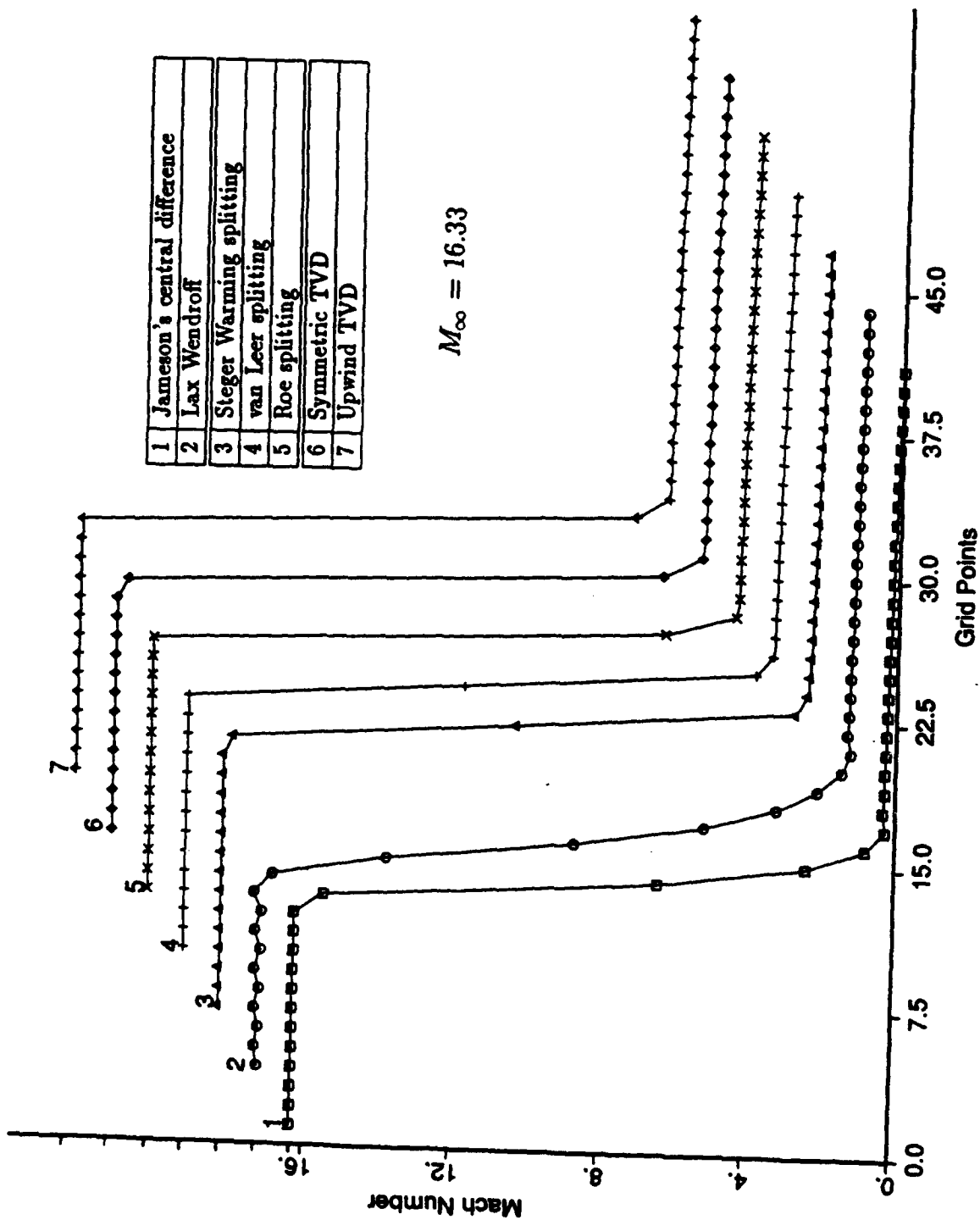


Figure 7: Mach number vs. grid point for a blunt body on a 40×40 grid at Mach 16.33 along the centerline.

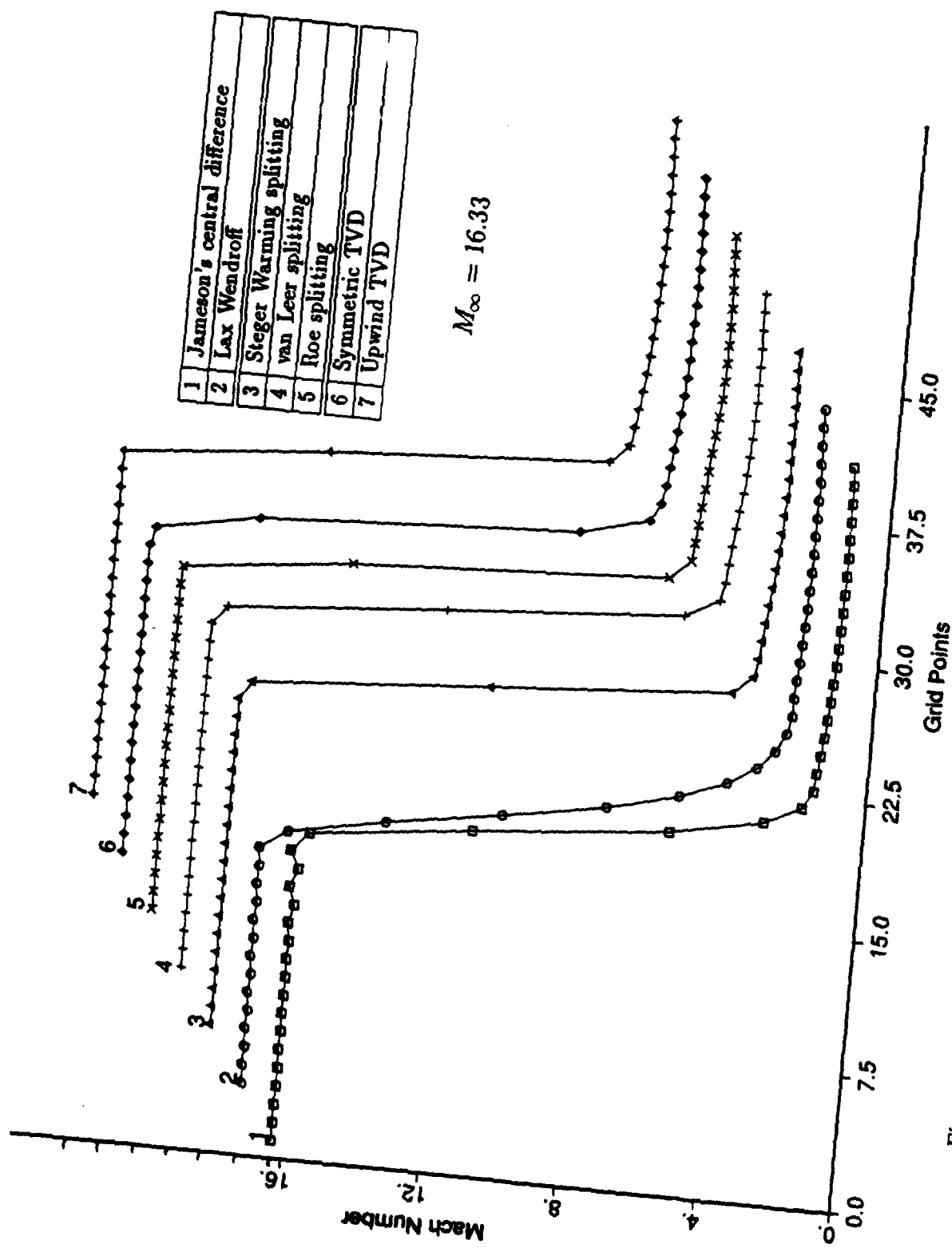


Figure 8: Mach Number vs. grid point for a blunt body on a 40×40 grid at Mach 16.33 along a ray inclined at 36° degrees to the vertical.

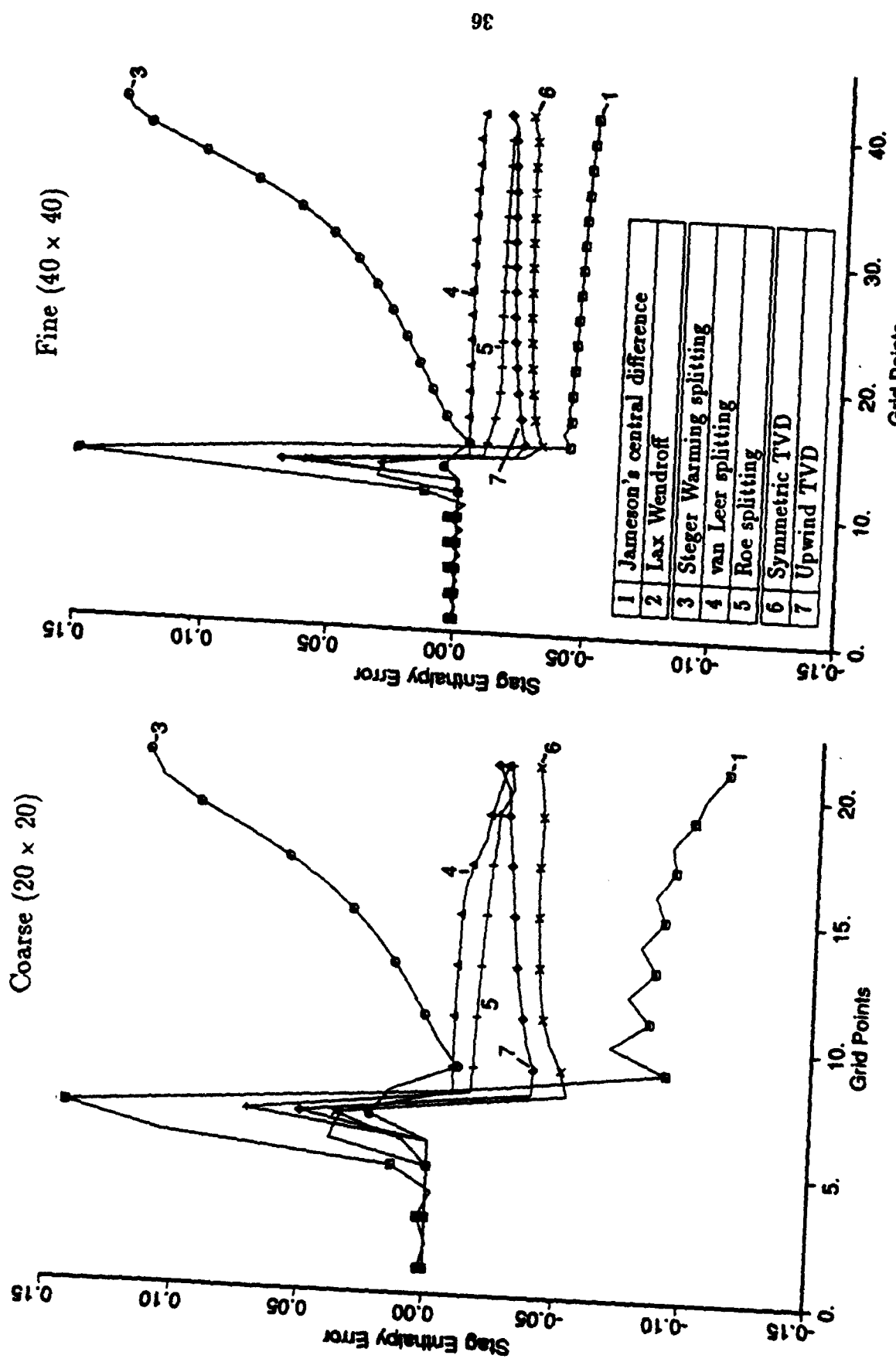


Figure 9: Stagnation enthalpy losses along the stagnation streamline on 20×20 and 40×40 grids for Mach 8.03.

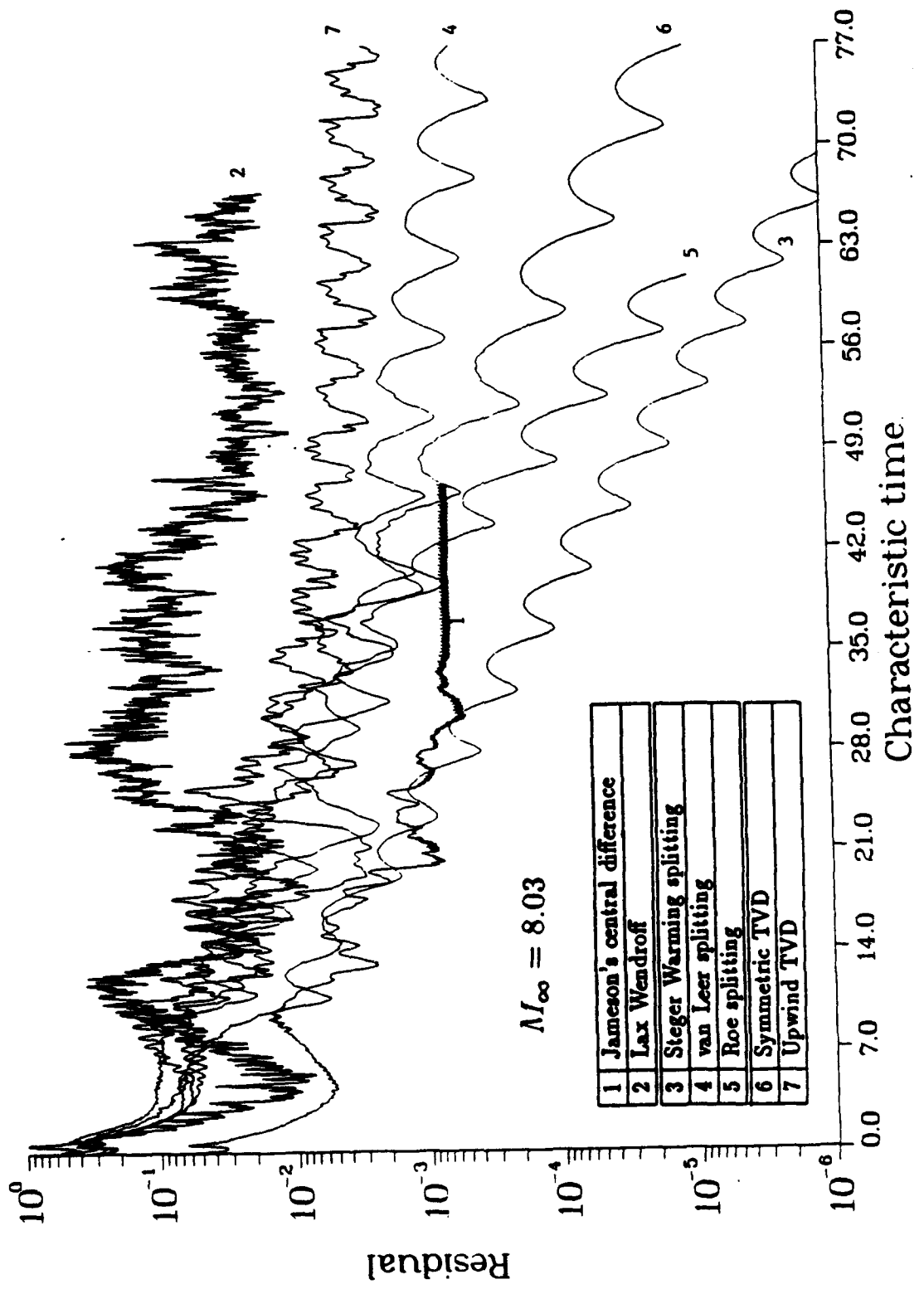


Figure 10: Residual convergence behavior for Type IV interaction on coarse (60 x 40) grid.

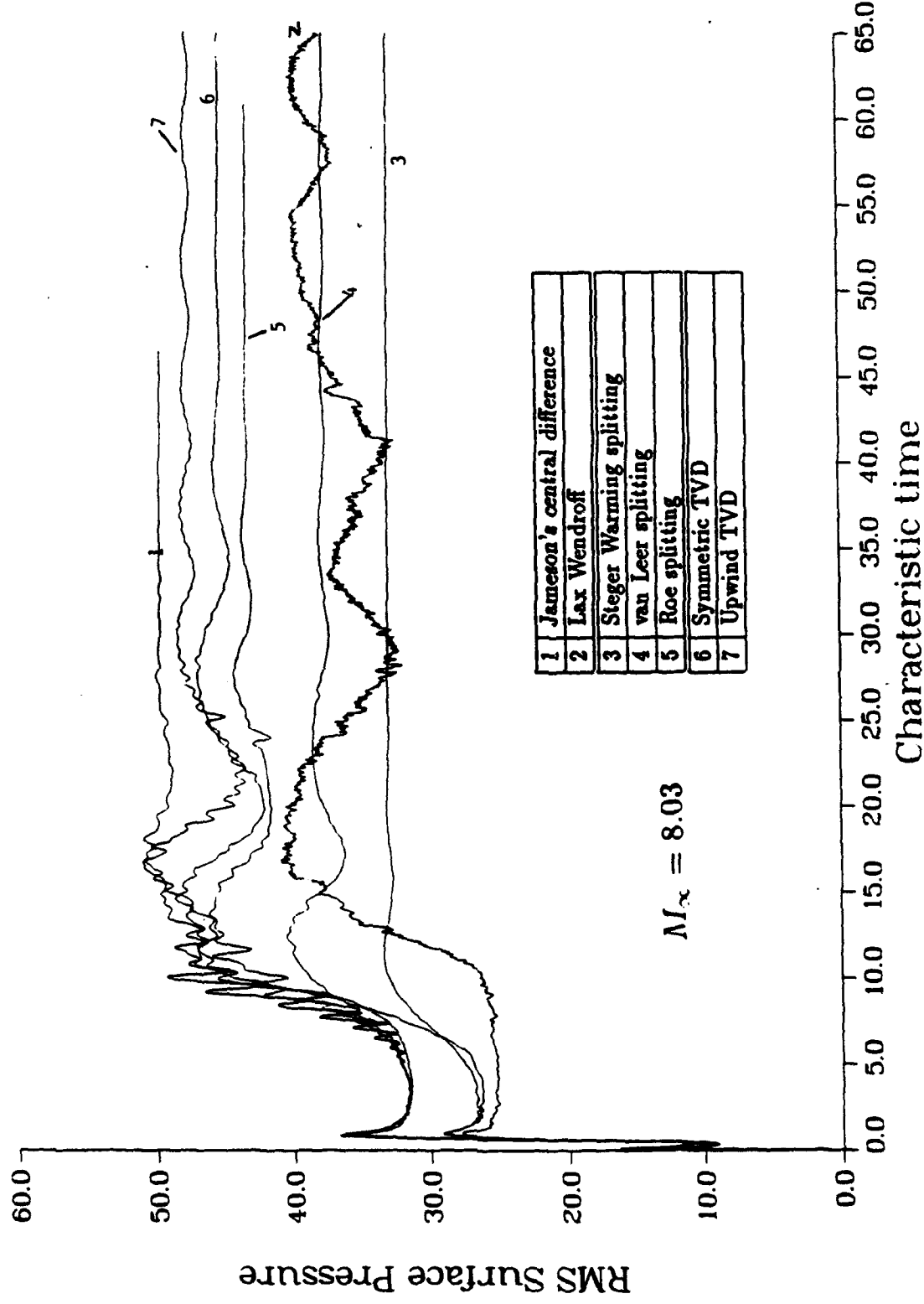


Figure 11: RMS surface pressure convergence behavior for Type IV interaction on coarse (60 x 40) grid.

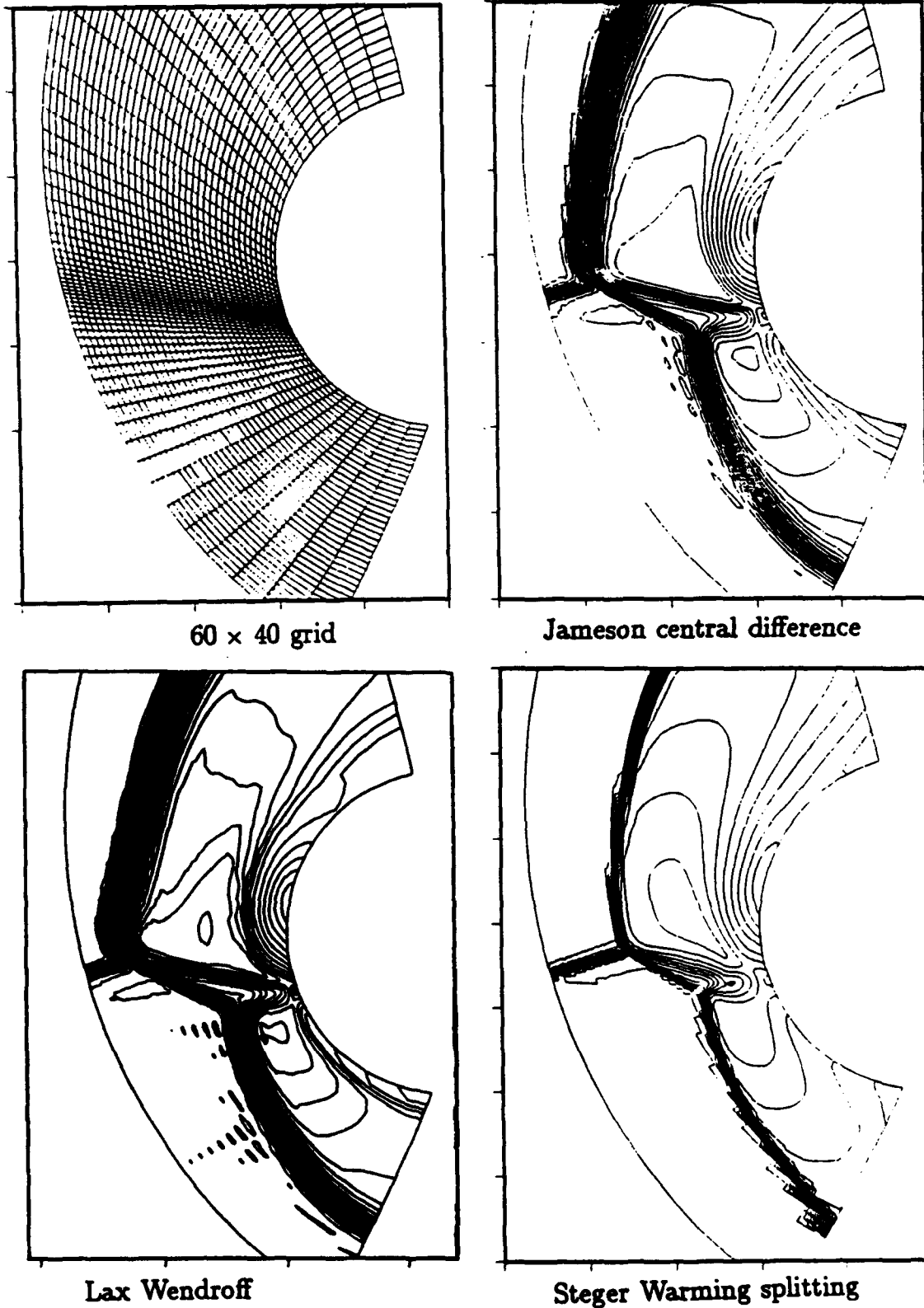
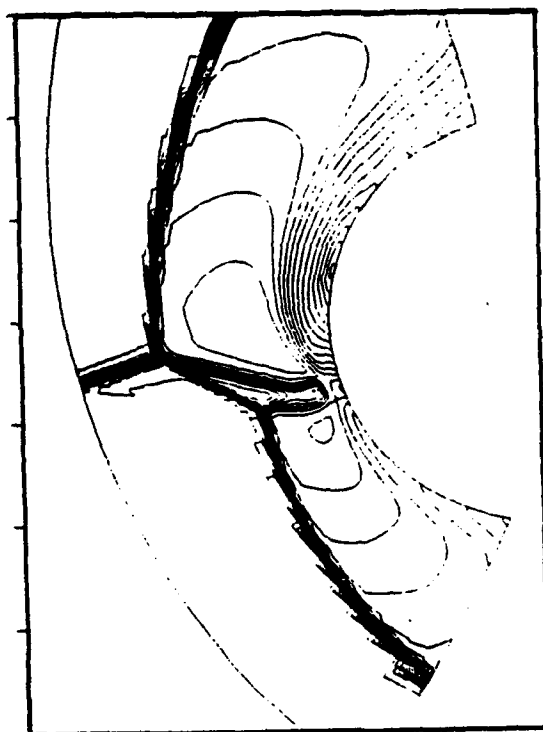
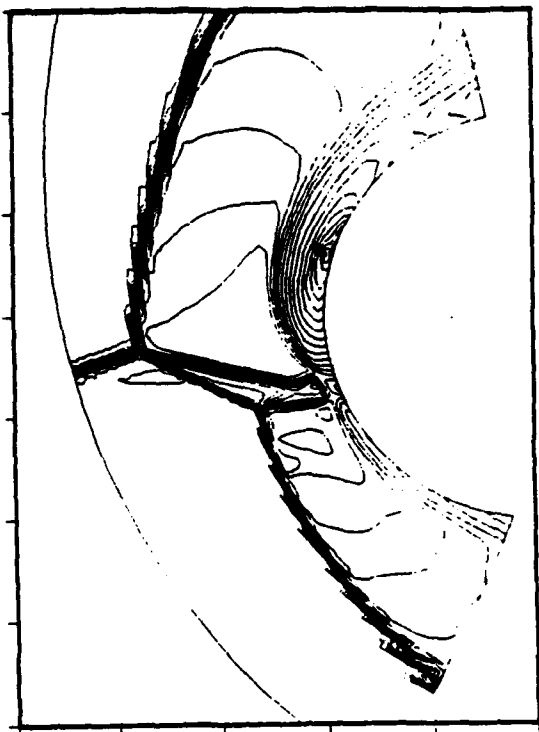


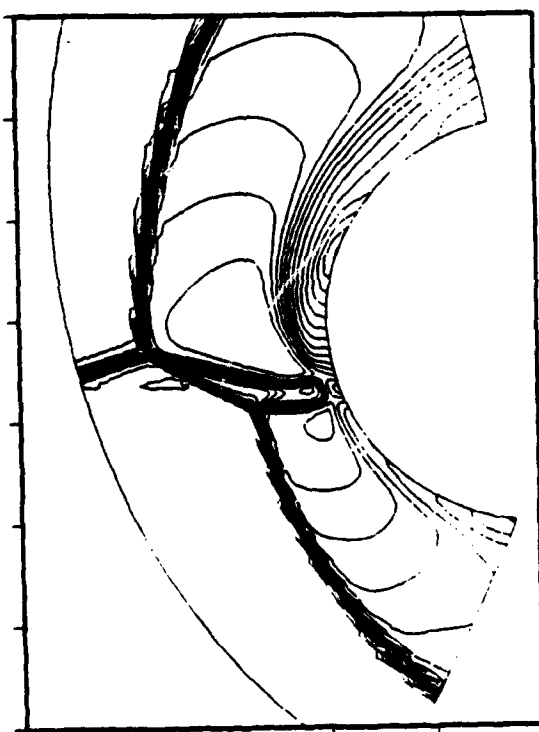
Figure 12: Mach contour plots for Type IV interaction on coarse (60 × 40) grid, $M_\infty = 8.03$



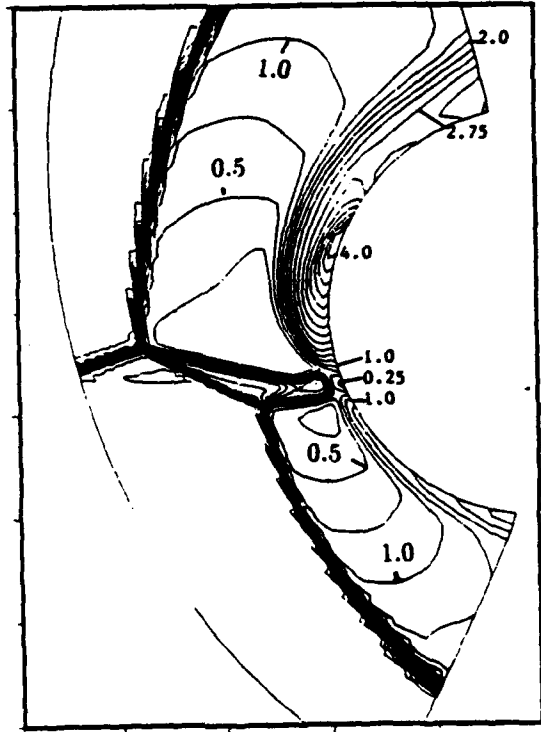
van Leer splitting



Roe splitting



Symmetric TVD



Upwind TVD

Figure 12: Mach contour plots for Type IV interaction on coarse (60×40) grid, $M_\infty = 8.03$
(continued)

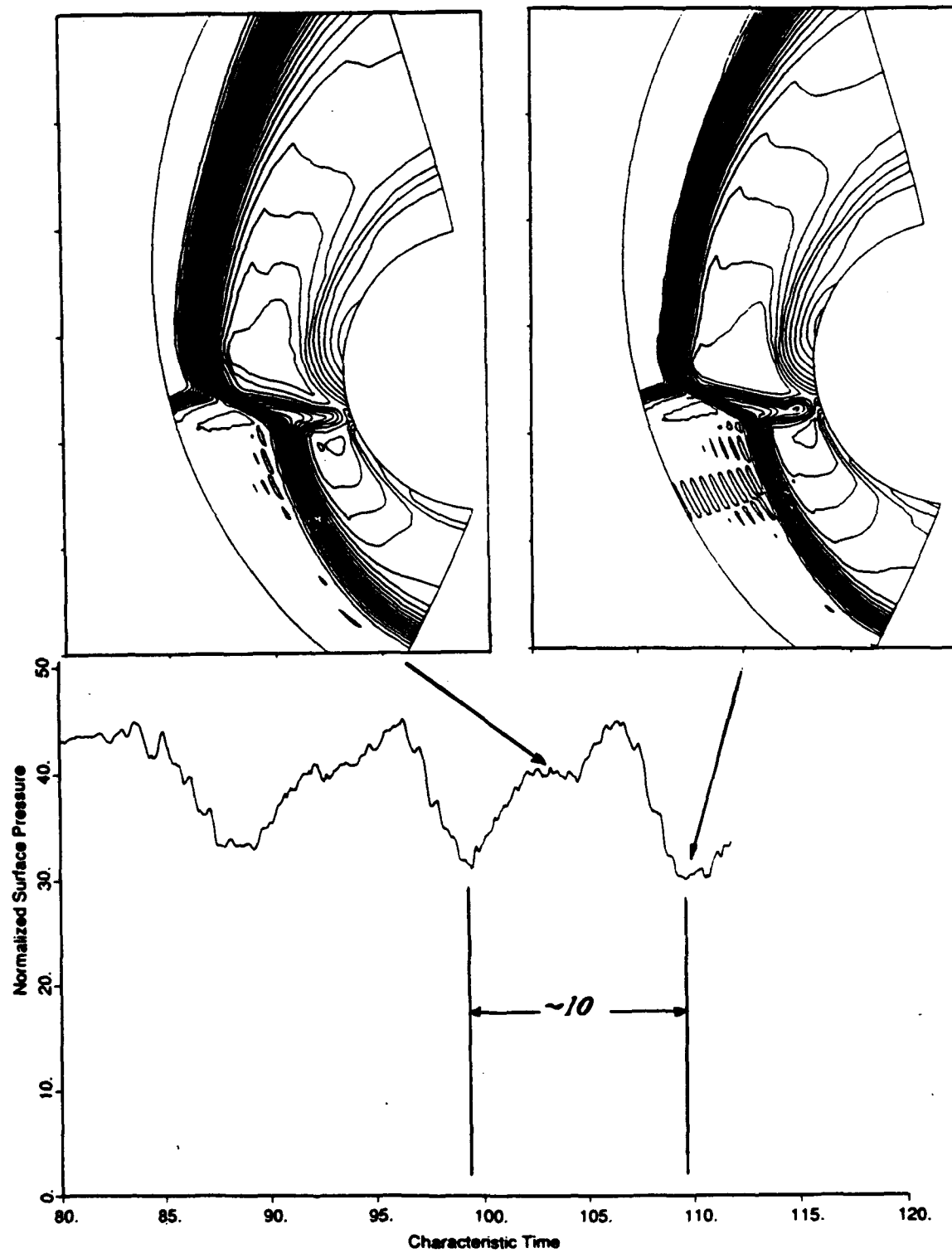


Figure 13: Mach contours at various extrema in convergence cycle for Lax-Wendroff scheme with dissipation reduced to blunt body levels and CFL number reduced by 10 (60×40 grid, $M_\infty = 8.03$).

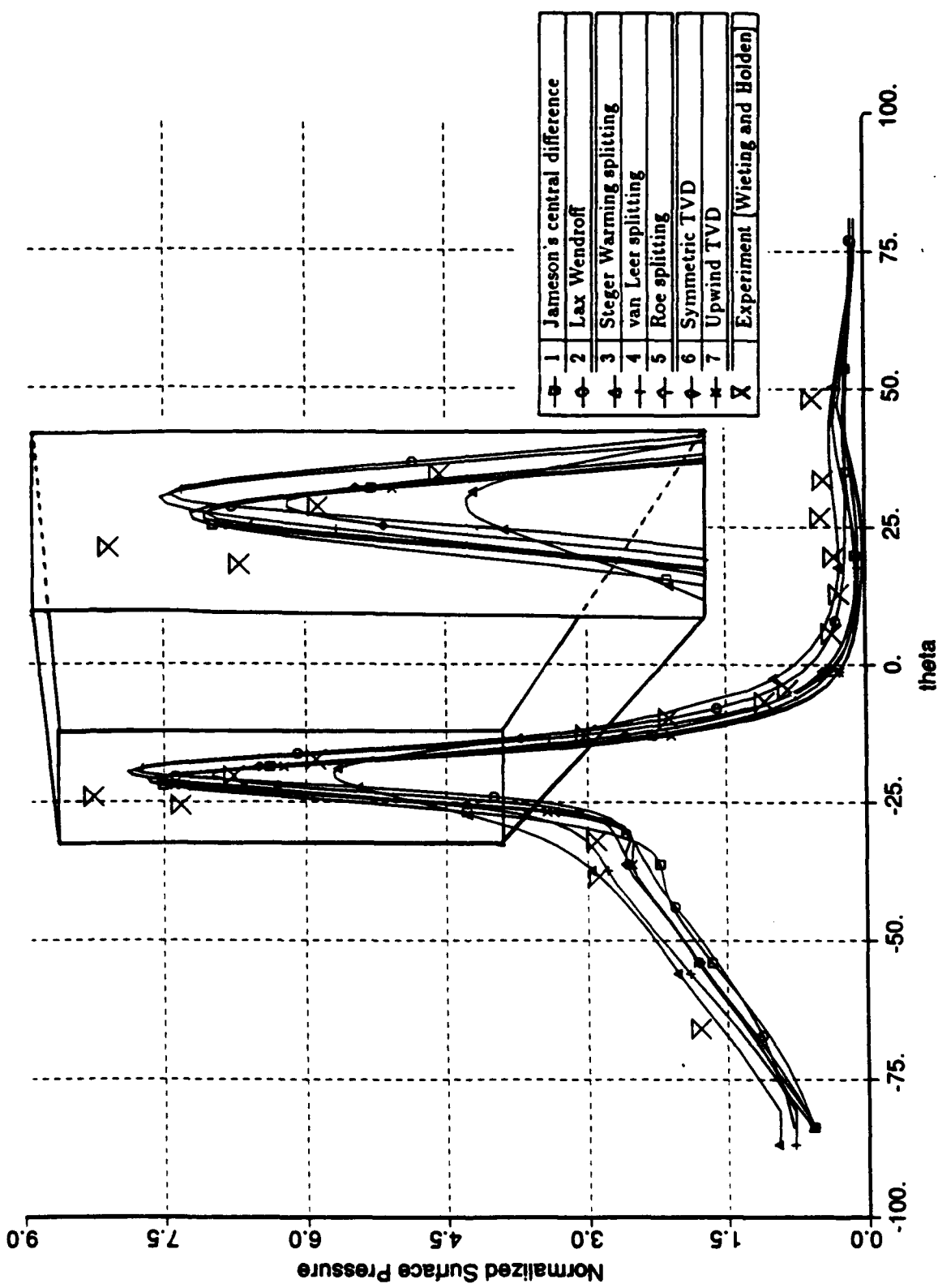


Figure 14: Surface pressure comparison for Type IV interaction on coarse (60 x 40) grid $M_\infty = 8.03$.

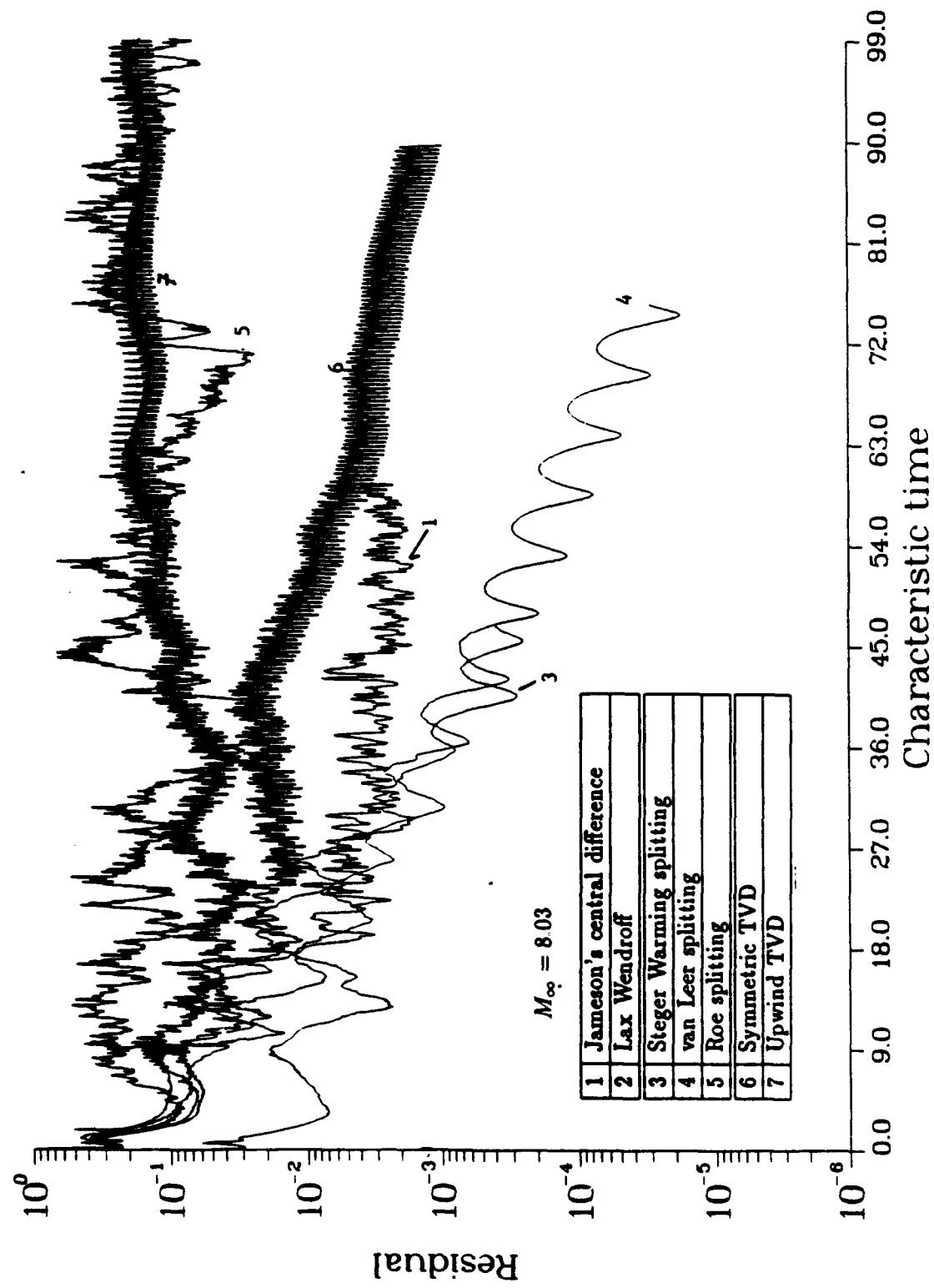


Figure 15: Residual convergence behavior for Type IV interaction on medium (120 x 80) grid,
 $M_{\infty} = 8.03$.

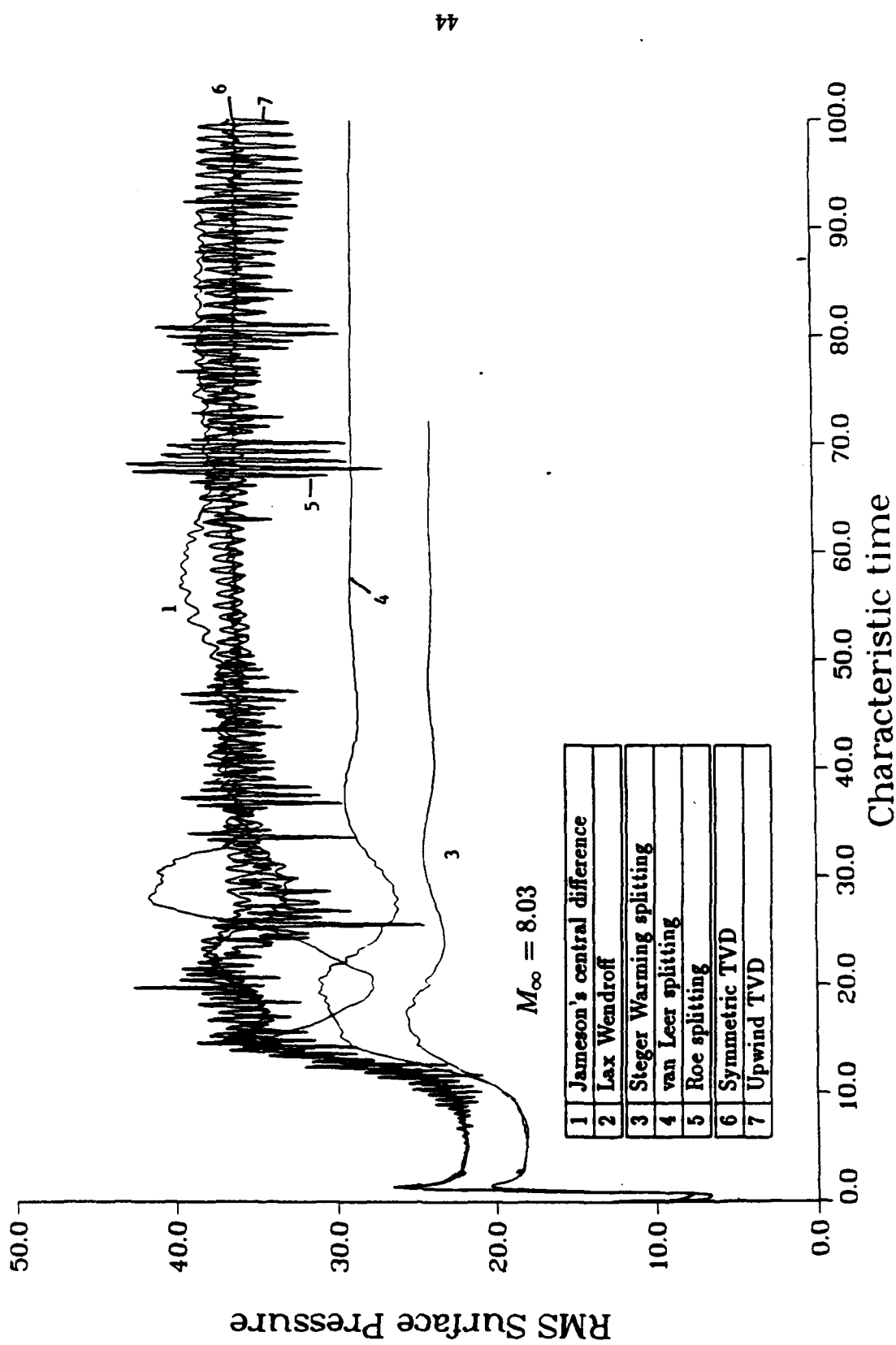


Figure 16: RMS surface pressure convergence behavior for Type IV interaction on medium (120 x 80) mesh, $M_{\infty} = 8.03$.

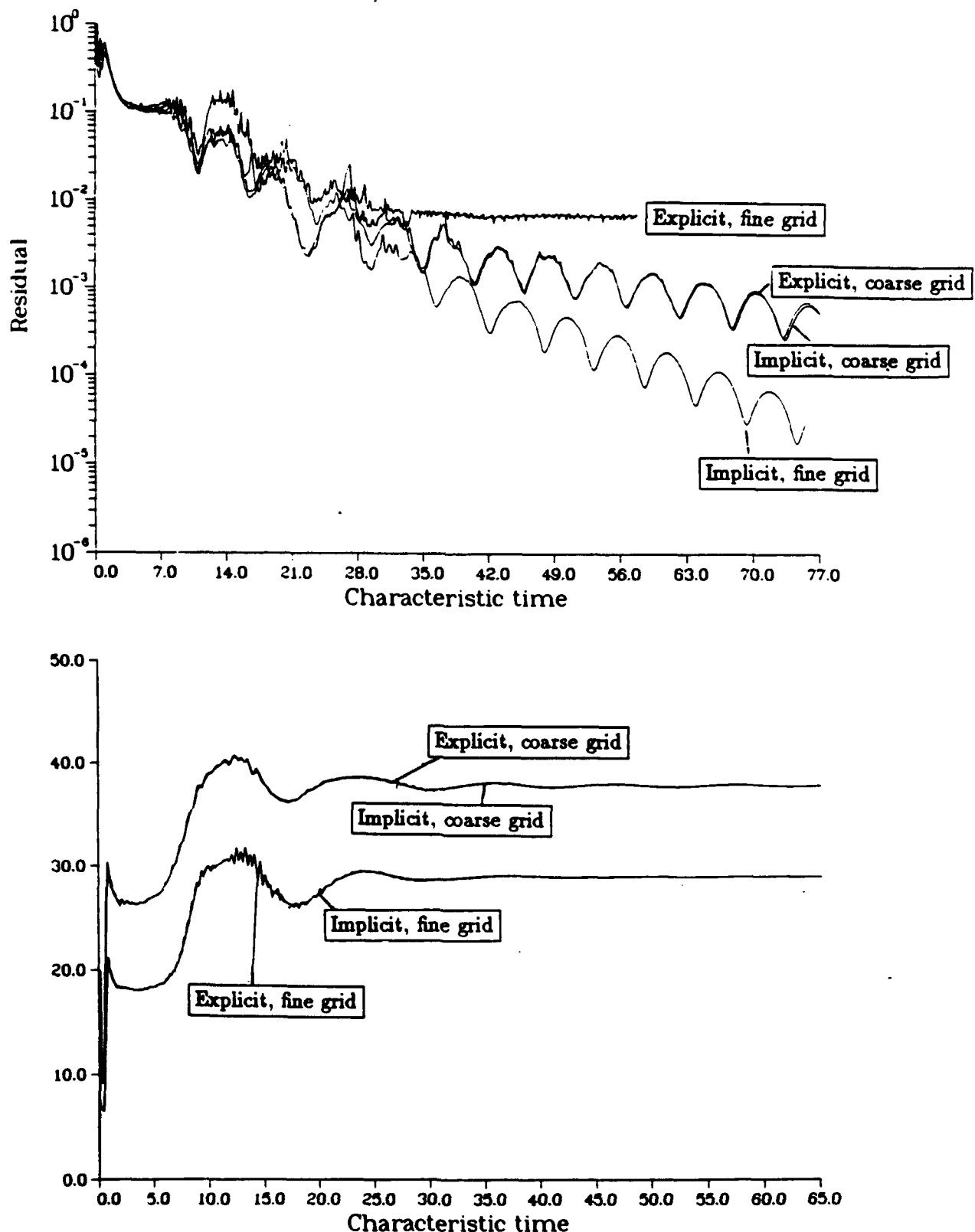
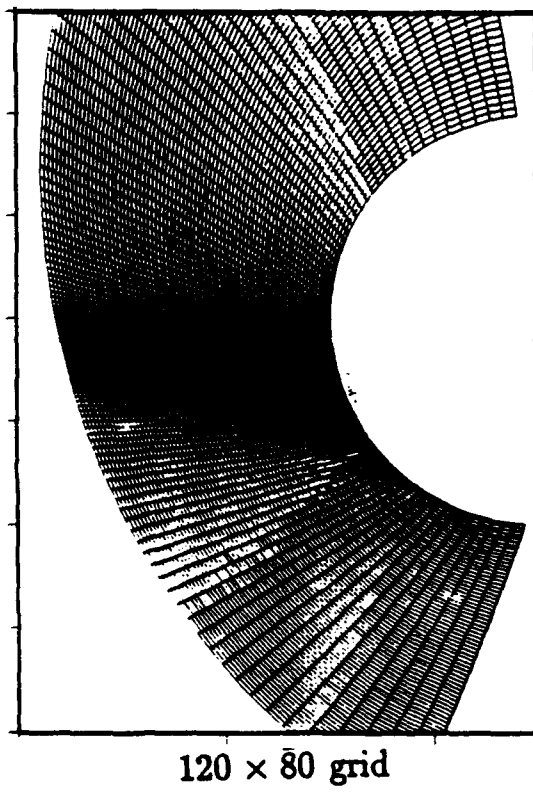
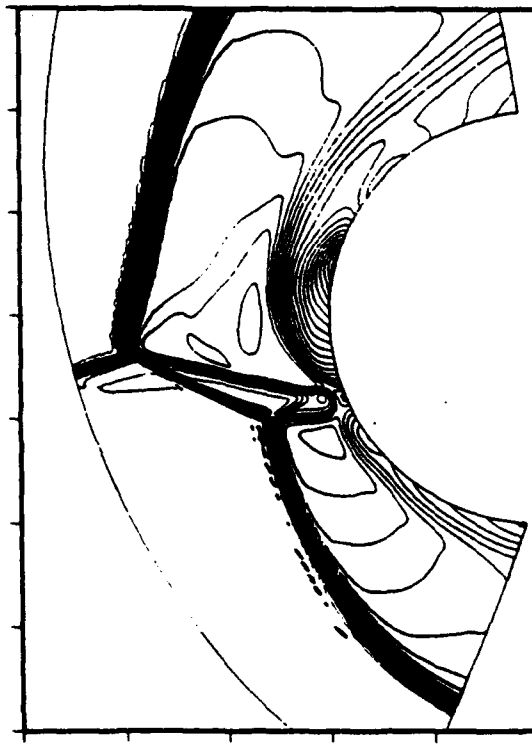


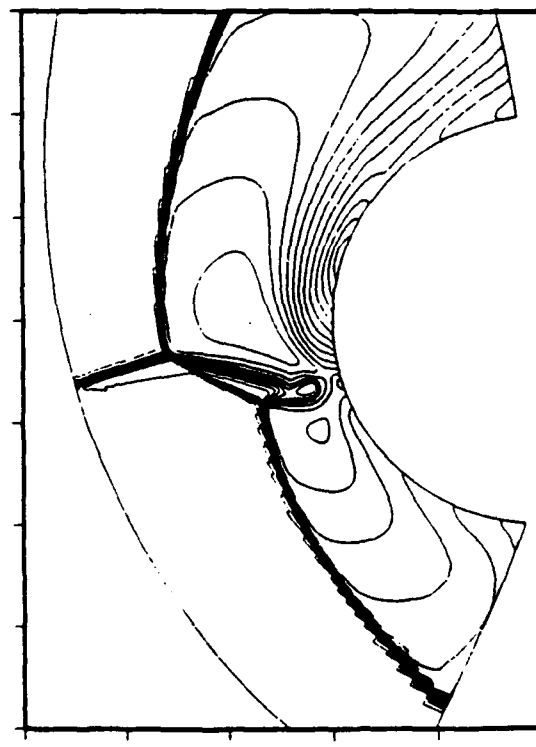
Figure 17: Convergence behavior of van Leer scheme with explicit and implicit time integration for Type IV interaction, $M_\infty = 8.03$.



120 \times 80 grid

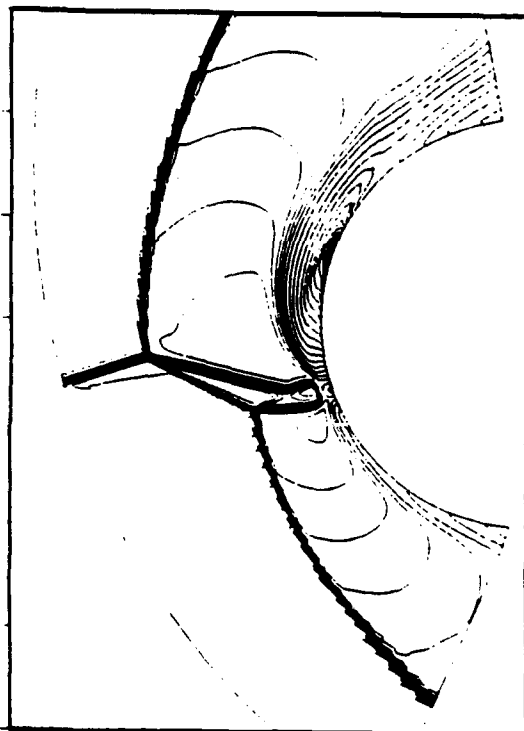


Jameson central difference

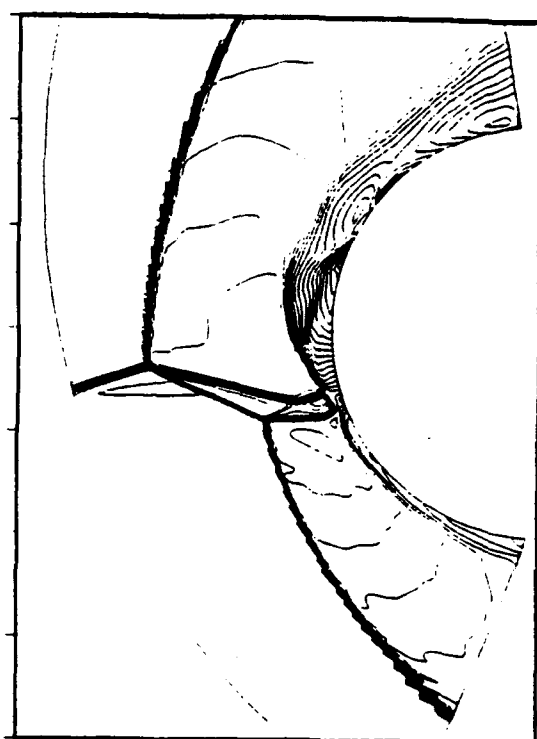


Steger Warming splitting

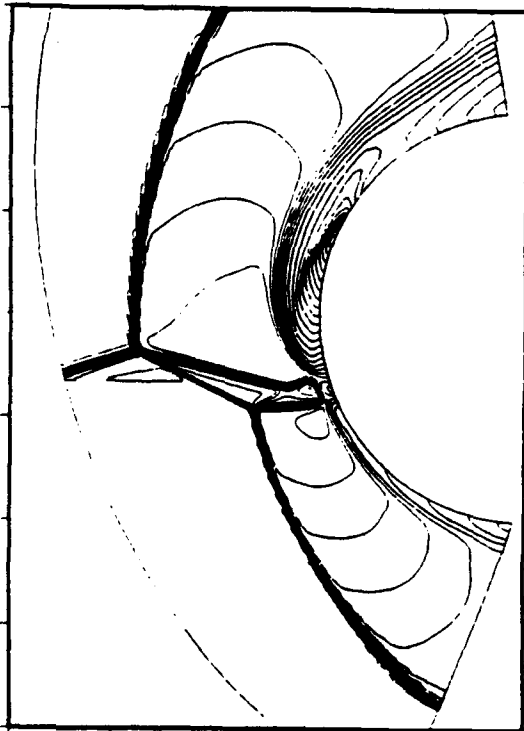
Figure 18: Mach contour plots for Type IV interaction on medium (120 \times 80) grid, $M_\infty = 8.03$



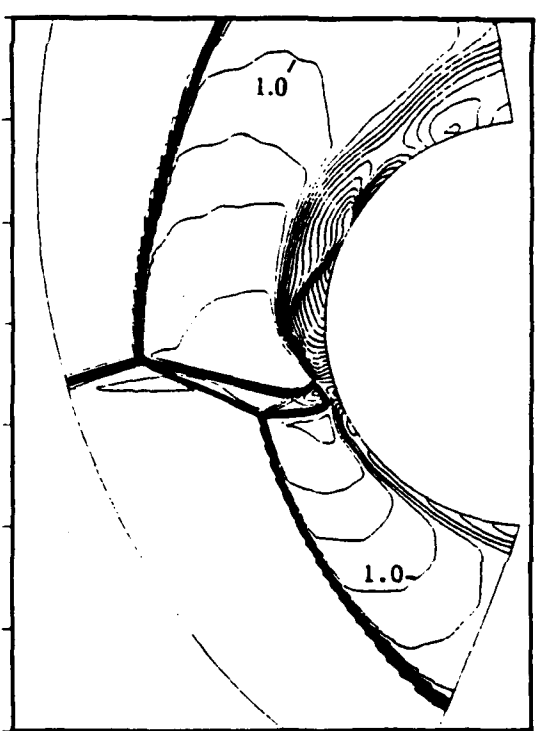
van Leer splitting



Roe splitting



Symmetric TVD



Upwind TVD

Figure 18: Mach contour plots for Type IV interaction on medium (120×80) grid, $M_\infty = 8.03$
(continued)

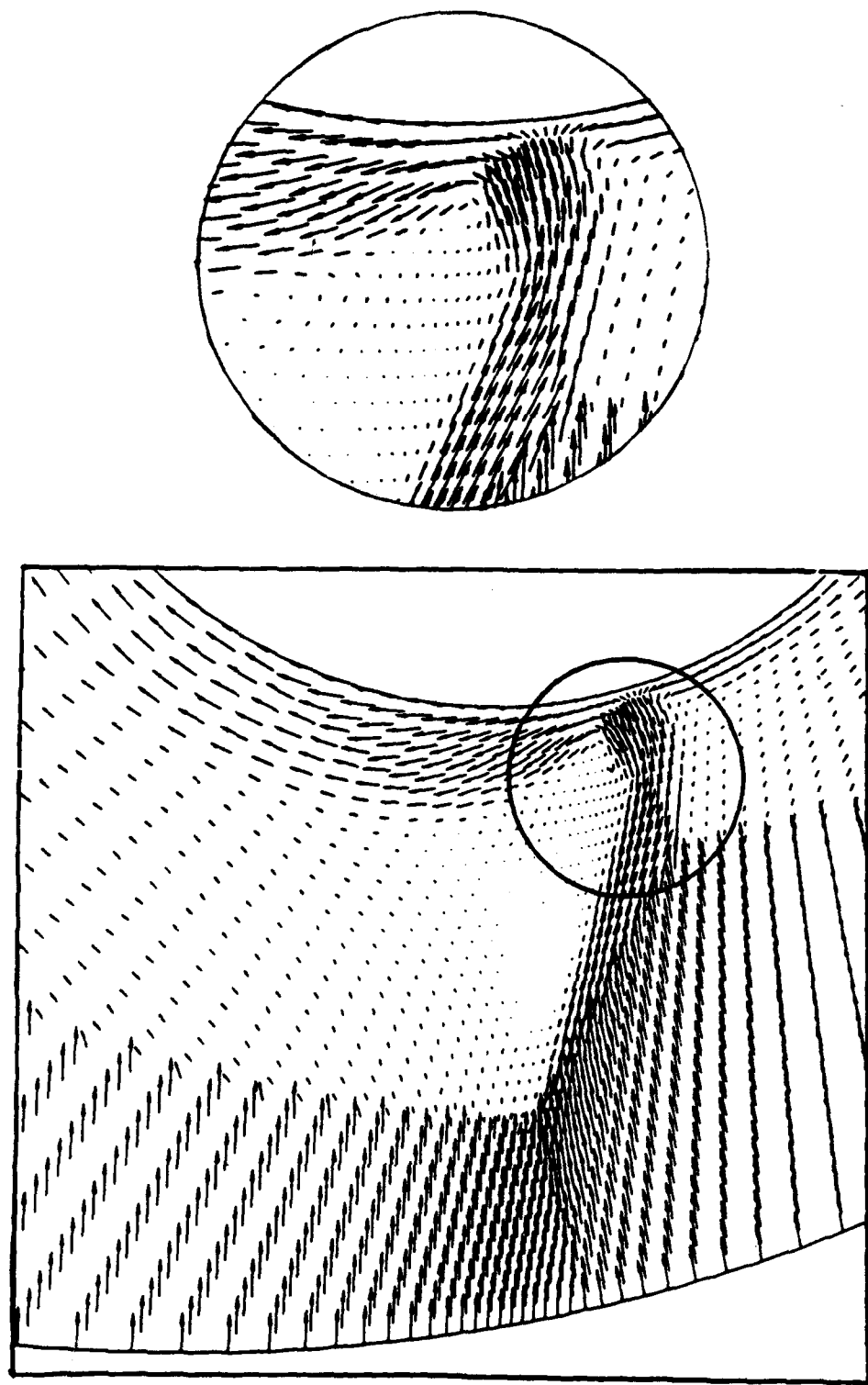


Figure 19: Velocity vectors of typical solution of Type IV interaction on a medium (120 x 80) grid (Upwind TVD), $M_{\infty} = 8.03$.

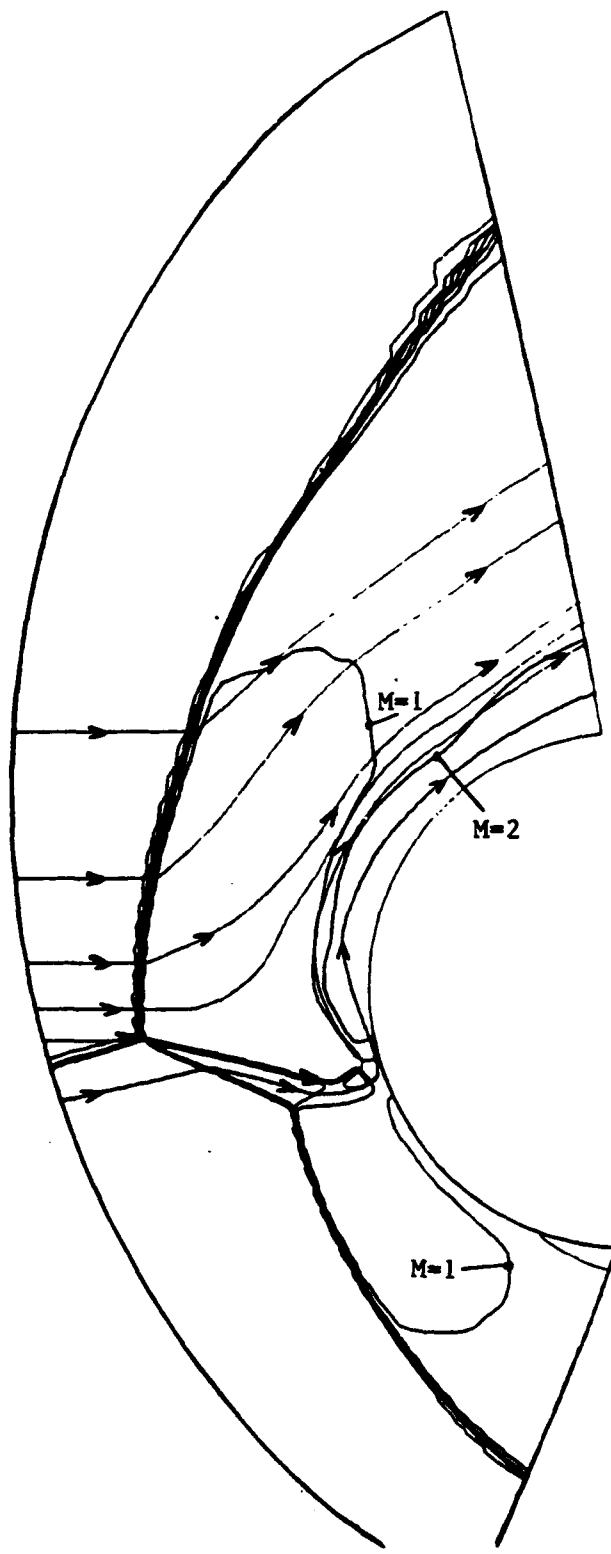


Figure 20: Representative “particle traces” from Upwind TVD scheme on medium (120 x 80) grid, $M_\infty = 8.03$.

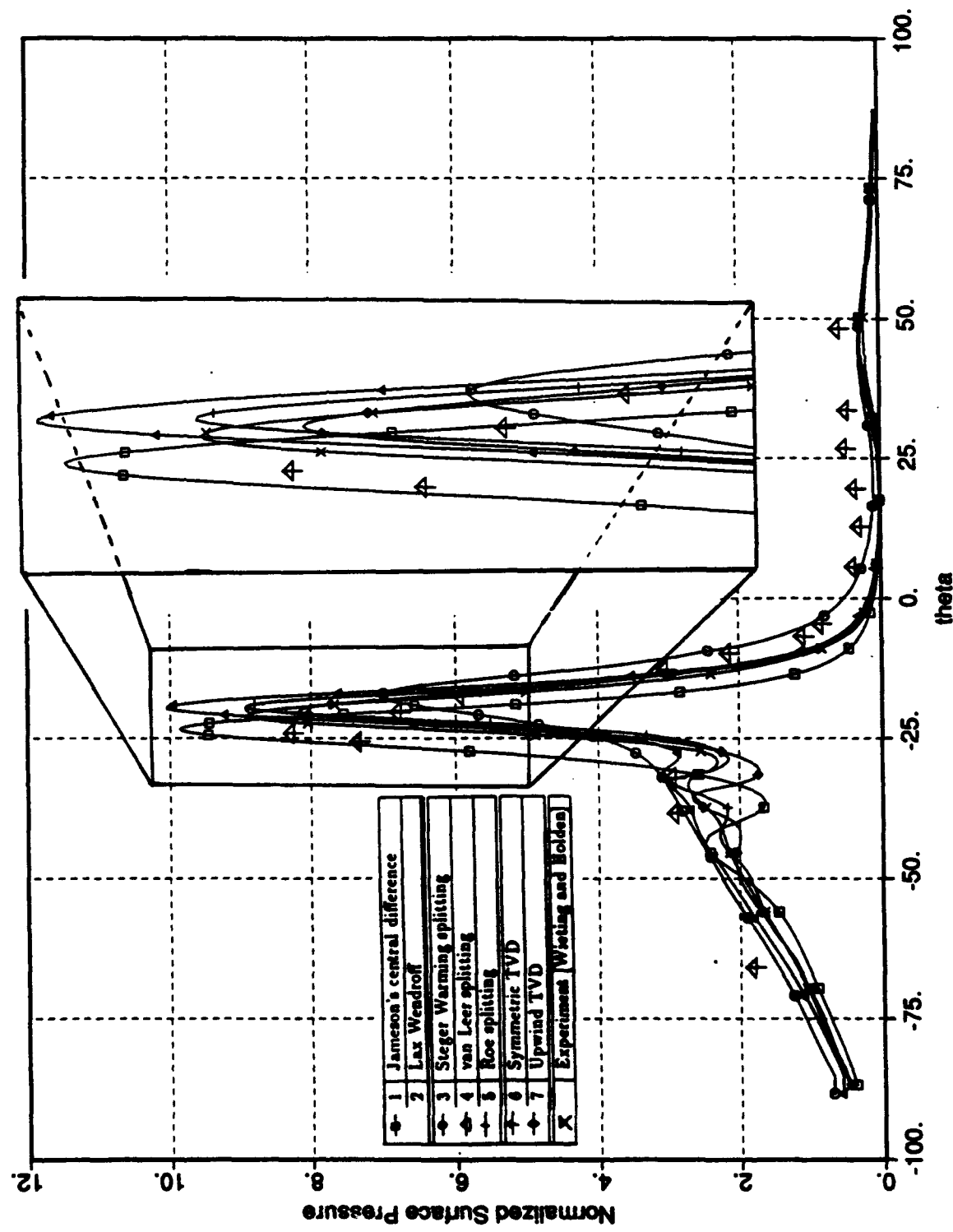


Figure 21: Surface pressure comparison for Type IV interaction on medium (120 x 80) grid,
 $M_\infty = 8.03$.

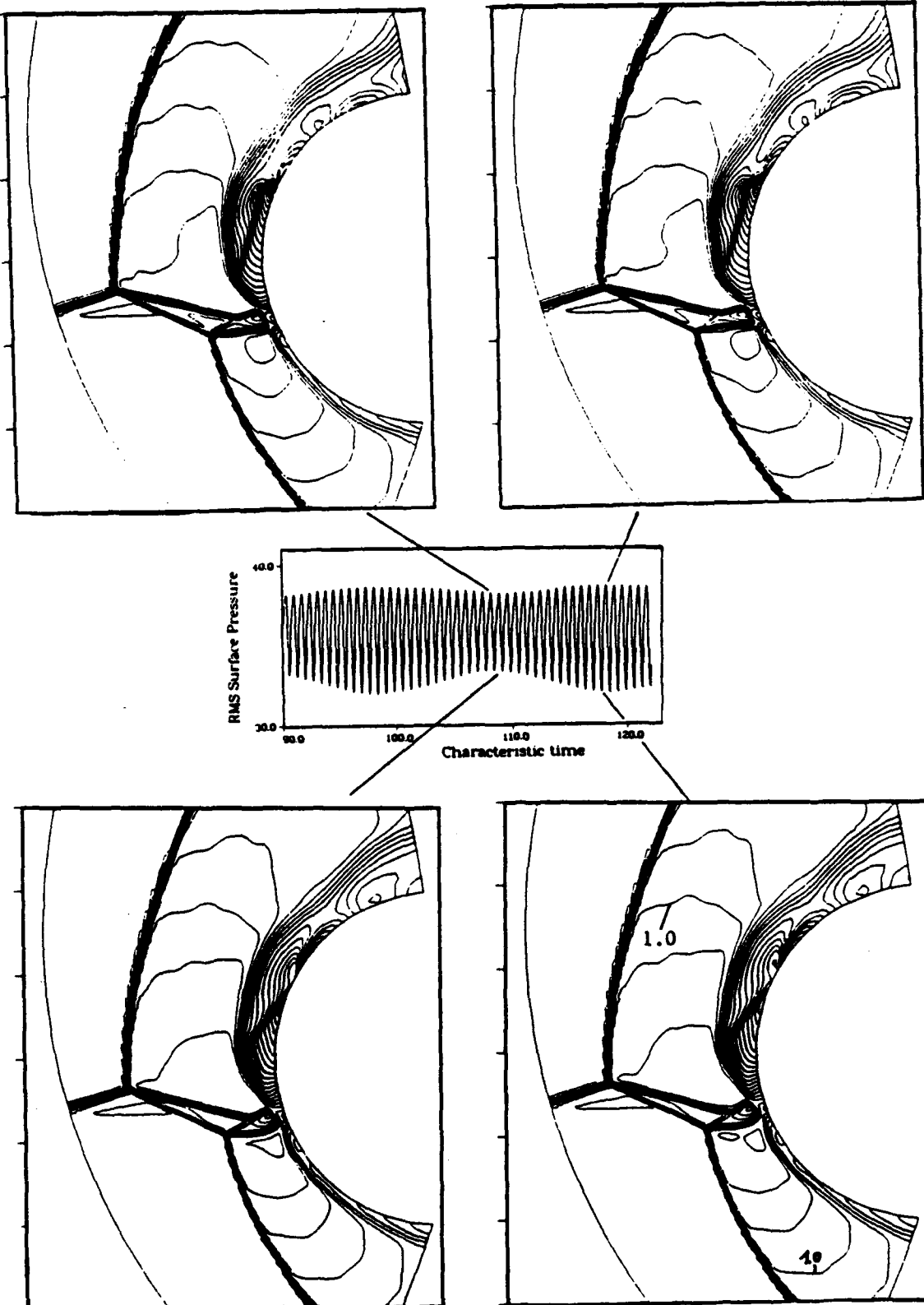


Figure 22: Mach contours at various extrema in convergence cycle for Upwind TVD scheme on medium (120×80) grid, $M_{\infty} = 8.03$.

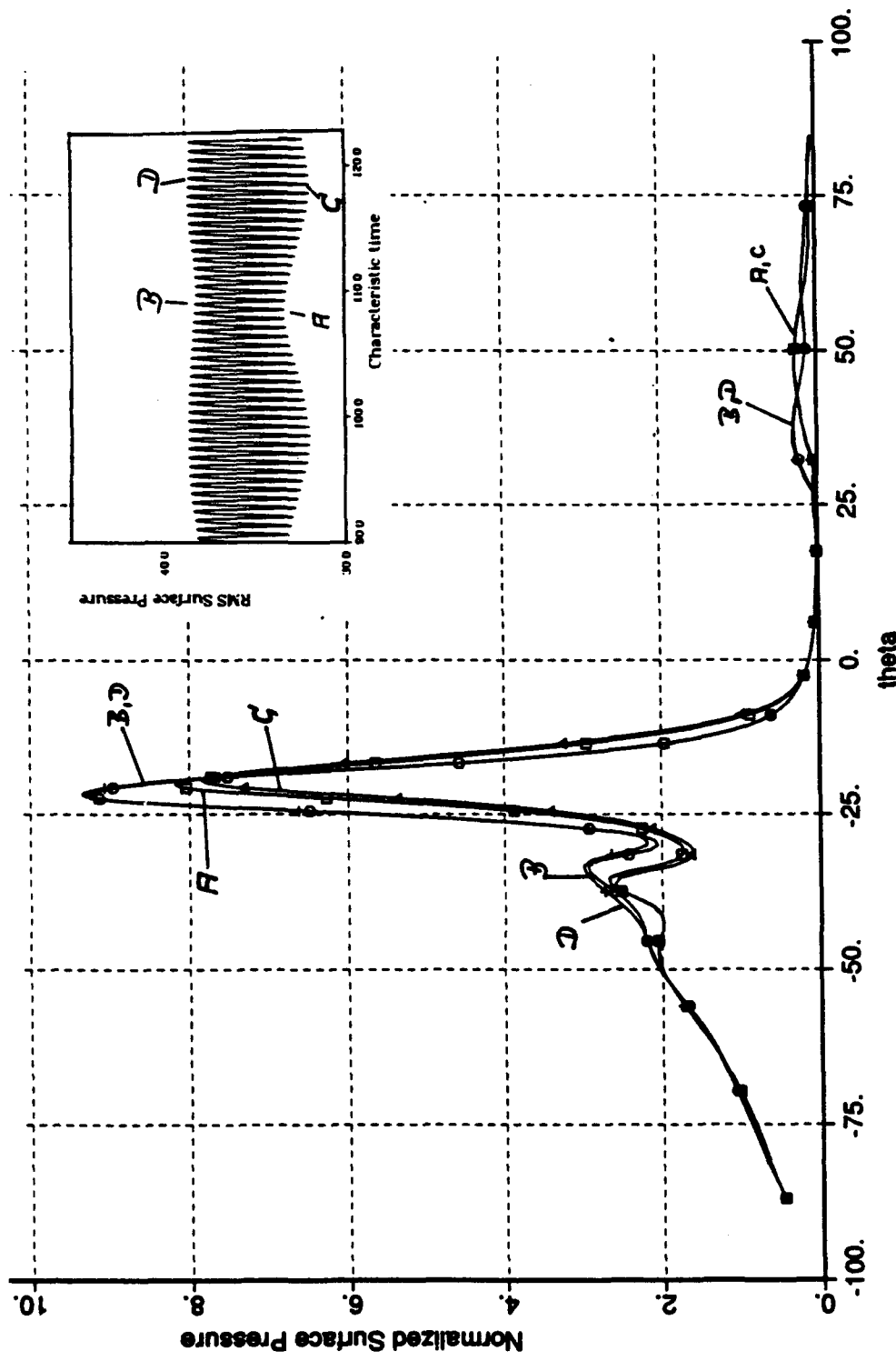


Figure 23: Surface pressure at various extrema in convergence cycle for Upwind TVD scheme on medium (120 x 80) grid, $M_{\infty} = 8.03$.

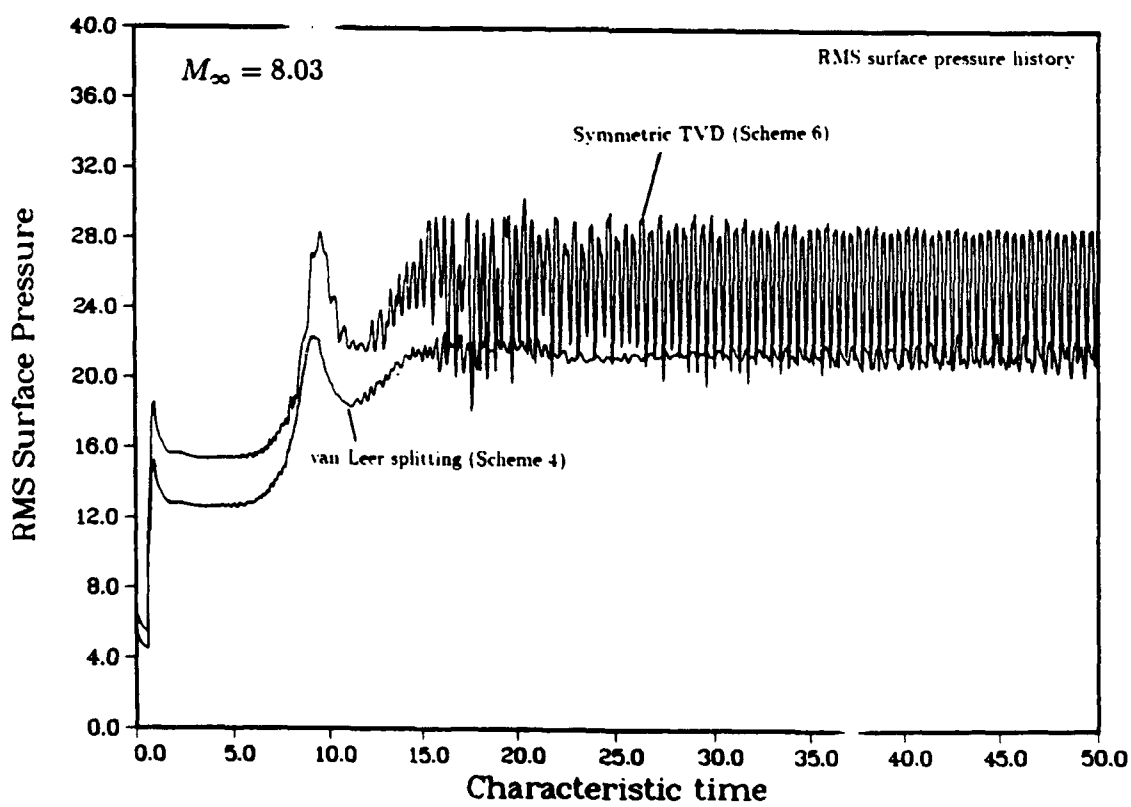
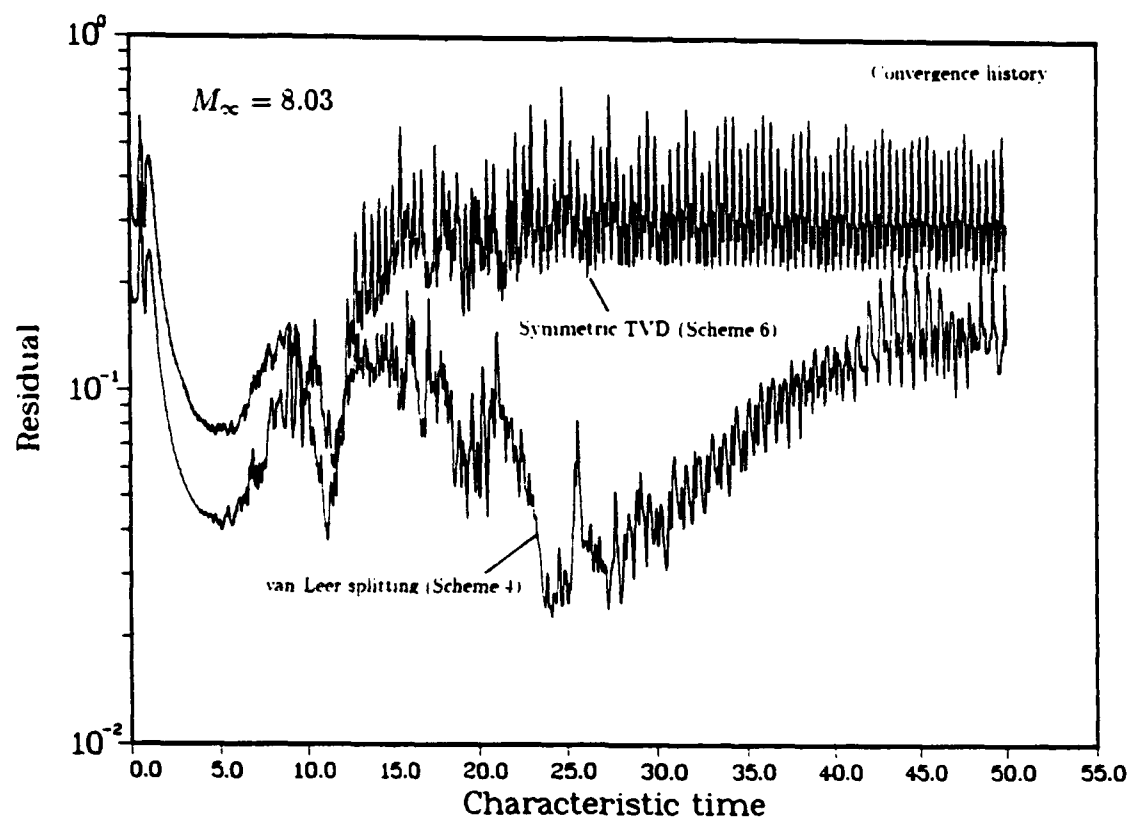


Figure 24: Convergence behavior for Type IV interaction on fine (240×160) grid, $M_\infty = 8.03$.
 Upper: Residual, Lower: RMS surface pressure.

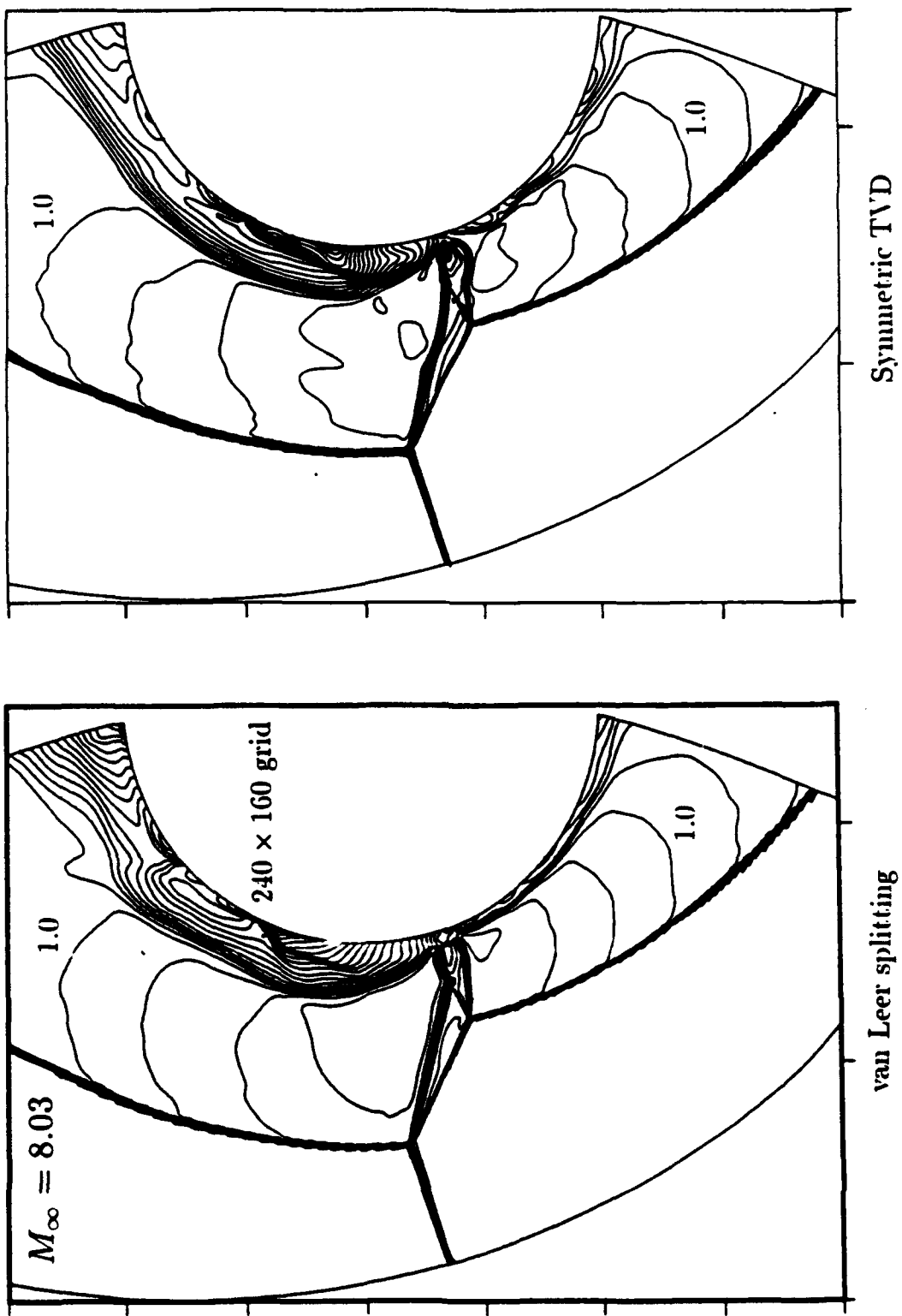


Figure 25: Mach contour plots for Type IV interaction on fine (240 x 160) grid for van Leer splitting and Symmetric TVD at 50 T_c , $M_\infty = 8.03$.

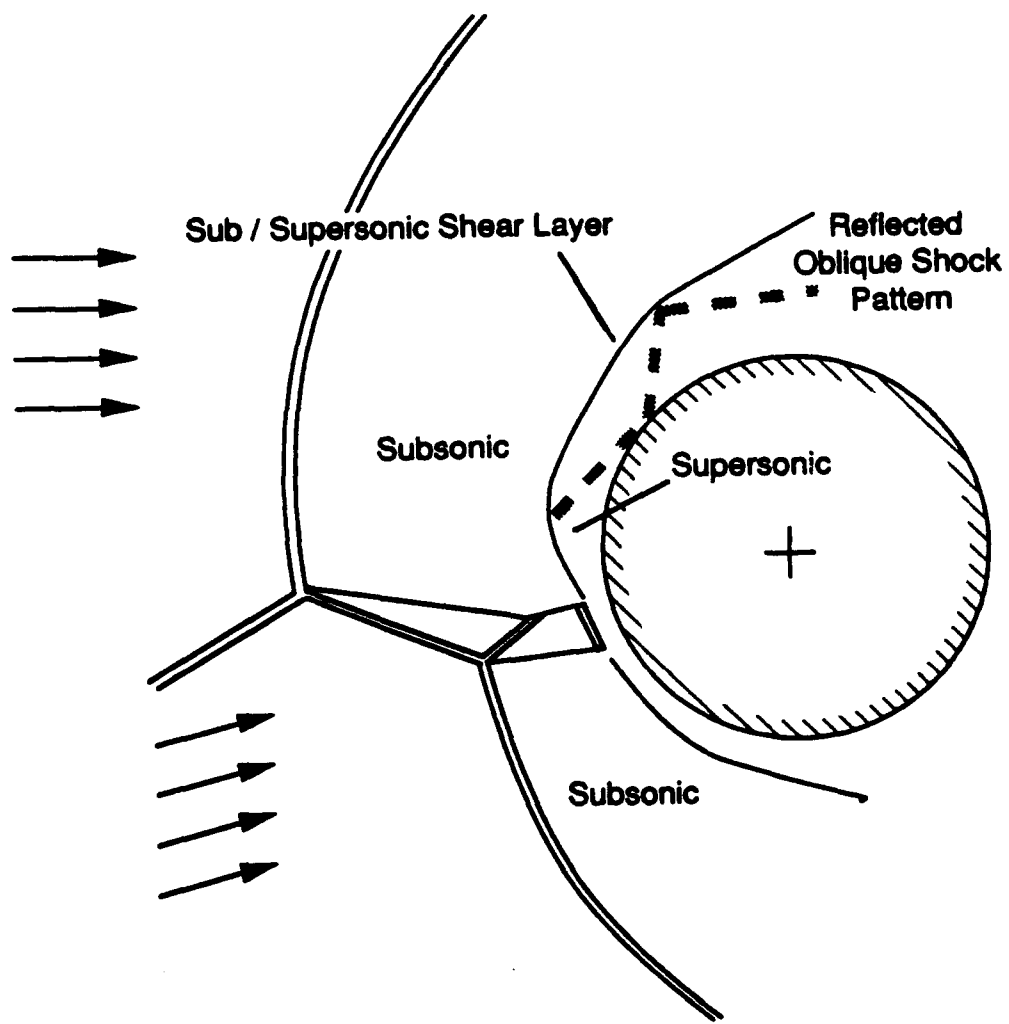


Figure 26: Schematic of solutions showing reflected oblique shock pattern in the supersonic layer over the body